Università degli studi di Pisa

Dipartimento di Fisica "E. Fermi"

Laurea Magistrale in Fisica

Sensitivity study of the CP asymmetry measurement in the $D^0 \to \pi^+\pi^-\pi^0$ decays on the Dalitz plot at Belle II

Supervisor

Prof. Giulia Casarosa

Candidate

Alessandro Terranova

ACCADEMIC YEAR 2024/2025

Contents

List of Figures

Introduction

One of the central open questions in modern physics is the observed dominance of matter over antimatter in the universe. According to Sakharov's conditions, the asymmetry between baryons and anti-baryons requires, among other ingredients, the violation of the CP symmetry.

Within the Standard Model (SM), CP violation (CPV) arises from the complex phase of the CKM matrix, a complex and non-diagonal matrix that describes quarks' mixing. CPV has been experimentally confirmed in the kaon and beauty sectors, and more recently in the charm sector, with a much smaller magnitude. However, the amount of CP violation predicted by the SM is insufficient to explain the baryon asymmetry of the universe, motivating the search for additional sources of CP violation.

The charm sector is particularly compelling in this context: D^0–$\bar{D}^0$ mesons system, being the only system made of up-type quarks where mixing occurs, provides a complementary probe to the strange and beauty sectors. In the SM, CP violation in charm decays has theoretical predictions affected by significant uncertainties due to non-perturbative QCD effects, and it is expected to be at most of the order of 10^{-3}, so any significantly larger effect would represent clear evidence of physics beyond the SM.

The goal of this work is to evaluate the statistical sensitivity to CP violation in the decay $D^0 \to \pi^+\pi^-\pi^0$ at Belle II, to assess the prospects for measuring it in the following years. This decay mode is of importance for several reasons. First, the $c \to ud\bar{d}$ transition is a Singly Cabibbo-Suppressed (SCS), a class of decays where CPV should be larger. Second, the decay proceeds predominantly via intermediate resonant states of two pions, giving rise to multiple interfering amplitudes, each of which can potentially show CP violation. Finally, the final state is common to both D^0 and $\bar{D}^0$, making it also sensitive to CP violation in the interference between decays with and without mixing.

The Dalitz plot (DP) is the key tool for studying such three-body decays. It is a phase-space representation in which the variables are the square of the invariant masses of final-state particle pairs. Its sensitivity to both weak and strong phases makes it possible to reveal CP violation in regions of the phase space, where global averaging could otherwise wash out the effect.

The observable sensitive to CPV that I have used is the CP asymmetry, defined as the ratio between the difference and the sum of the number of correctly reconstructed D^0 and $\bar{D}^0$ decays. To identify the regions of the DP that are more sensitive to CPV, I analysed a recent article that predicts the value of the CP asymmetry on the DP. The CP asymmetry prediction is based on a $\Delta U = 0$ rule theory, which affirms that decays with a null variation of U-spin (a SU(2) subgroup of SU(3)$_{flavour}$, that connects the down and the strange quarks) are favoured with respect to decays with $\Delta U = 1$.

My analysis is based on the simulated dataset produced by the Belle II collaboration. The Belle II experiment, located in Tsukuba (Japan), collects data at the SuperKEKB collider. SuperKEKB is a high-luminosity B factory that operates at the center of mass energy at or below the mass of the $\Upsilon(4S)$ resonance. The experiment has collected more than 550 fb^{-1} in the last six years and will restart data taking before the end of the year, with the goal of collecting 50 ab^{-1}.

After applying the selection criteria, I conducted an initial study to assess the reconstruction efficiency, in terms of the kinematic variables of the decay, in different portions of the Dalitz plot.

I have selected the regions on the DP based on the results of the paper mentioned above. The regions of interest are dominated by the contributions of the $\rho^{\pm}(770)$ resonances and by their mutual interference. Then, averaging the numerical values of CP asymmetry predicted in the reference study with the Belle II dataset, I computed the expected average CP asymmetry over different reduced portions of the Dalitz plot, therefore also including the reconstruction efficiency. I have then evaluated the statistical uncertainty of the average predicted asymmetry in the specific portions of the Dalitz plot. I extrapolated it for different values of integrated luminosity to determine the significance of the expected measurement.

The thesis is organized as follows:

- Chapter 1: Introduction to the Standard Model and the phenomenon of neutral meson mixing, the role of CP violation in this context.
- Chapter 2: Discussion on the Dalitz Plot as a tool to investigate CP Violation in three-body decays, in particular the signal channel $D0 \to \pi^+\pi^-\pi^0$; a theoretical prediction of CP asymmetry for the $D0 \to \pi^+\pi^-\pi^0$ decay on the Dalitz plot.
- Chapter 3: The introduction to the Belle II experiment, and experimental challenges for the measurement of the CP asymmetry in $D0 \to \pi^+\pi^-\pi^0$ channel decay.
- Chapter 4: Estimation of the expected value of the CP asymmetry from the theoretical paper for an hypothetical measurement at Belle II. Estimation of its statistical significance for different regions of the Dalitz plot and integrated luminosities, and estimation of the luminosity that would be required to achieve target sensitivity levels.
- Chapter 5: Prospects of possible future development of this analysis and conclusions.

Chapter 1

CP violation in the Standard Model

In this first chapter, the theoretical framework of the Standard Model is introduced, with a focus on quark mixing, the phenomenon of neutral mesons mixing, and the role of CP violation in this context.

1.1 CP Violation and the Matter–Antimatter Asymmetry

The strong, weak, and electromagnetic interactions are the fundamental forces that govern the subnuclear world. The Standard Model is currently the most comprehensive and experimentally validated theoretical framework describing these interactions among elementary particles. However, several observations remain unexplained within the Standard Model, among which the observed asymmetry between matter and antimatter is one of the most significant.

As far as we know, the Universe we observe today is overwhelmingly dominated by matter. There is no evidence for the existence of anti-galaxies or anti-clusters [1], and various studies in gamma-ray astronomy have constrained the possible presence of large domains of antimatter [2–4].

According to the Sakharov conditions [5], the generation of such an asymmetry from an initial state of thermal equilibrium requires, among other ingredients, the violation of Charge-Parity (CP) symmetry. Although CP violation (CPV) has been firmly established within the Standard Model, the magnitude of CPV predicted by the CKM mechanism is insufficient to account for the observed asymmetry between matter and antimatter. This strongly motivates the search for additional sources of CP violation beyond the Standard Model.

In this thesis, a search for CP violation in the charm sector is discussed, particularly in the decay channel $D^0 \to \pi^+\pi^-\pi^0$.

1.2 Introduction to the Standard Model

The Standard Model (SM) is a quantum field theory that describes the kinematics and the dynamics of fundamental particles. These elementary particles are classified as fermions, which are the constituents of matter, and bosons, which mediate the interactions.

Fermions and Bosons

In the Standard Model, there are twelve fermions, organized in three generations, each consisting of a quark doublet and a lepton doublet. For each fermion, there exists a corresponding antiparticle, as shown in Figure 1.1.

Quarks interact via the electromagnetic, weak, and strong forces. They carry one of three possible colour charges, have electric charges of either $\frac{2}{3}$ or $-\frac{1}{3}$, and come in six flavours: up (u), down, (d), charm (c), strange (s), top (t) and bottom (b).

Leptons, instead, do not carry colour charge and therefore do not participate in strong interactions. The charged leptons - the electron (e^-), the muon (μ^-), and the tauon τ^- - interact through both the electromagnetic and weak forces. The neutral leptons, or neutrinos - the electron neutrino (ν_e), muonic neutrino (ν_μ) and tauonic neutrino (ν_τ) - interact exclusively via the weak interaction.

Four gauge bosons mediate the interactions among these fermions: the photon (γ) mediates the electromagnetic interaction, the $W^\pm$ and Z^0 bosons are responsible for the weak interaction, and eight gluons (g) mediate the strong interaction between quarks through the exchange of colour charge. Additionally, the Higgs boson (H) gives masses to the W and Z bosons and, through Yukawa couplings, to the fermions.

1.3 The Standard Model Formalism

It is important to provide a brief introduction to the Standard Model formalism in order to establish a clear framework for the topics that will be discussed in the following chapters.

1.3.1 The Standard Model Lagrangian

The SM Lagrangian [7, 8] can be divided in 4 contributions:

$$\mathcal{L}_{SM} = \mathcal{L}_{QCD} + \mathcal{L}_{EW} + \mathcal{L}_{Higgs} + \mathcal{L}_{Yukawa} \tag{1.1}$$

and it is invariant under the gauge group, which will be introduced and analysed later in this chapter,

$$SU(3)_C \otimes SU(2)_L \otimes U(1)_Y \,.$$

Fermions are assumed to be massless. Their masses will be introduced later. Unless otherwise specified, fermions are eigenstates of the interaction.

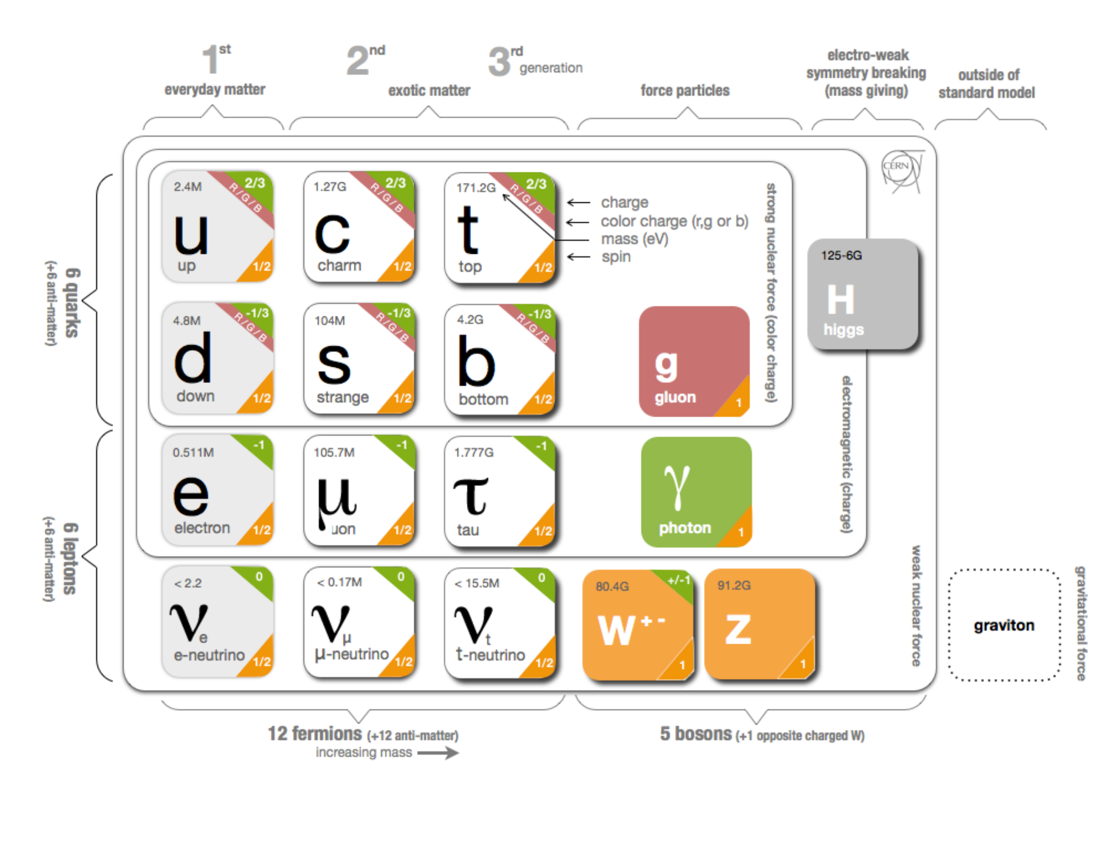

Figure 1.1: The particle content of the Standard Model [6]

The Strong Term: $\mathcal{L}_{QCD}$ and $SU(3)_C$

The colour group $SU(3)_C$ describes the symmetry of the Quantum Chromodynamics (QCD): the strong interaction gauge theory. The Lagrangian of the QCD is

$$\mathcal{L}_{QCD} = i\,\bar{Q}\,\not{\mathcal{D}}\,Q - \frac{1}{4}G^a_{\mu\nu}(G^a)^{\mu\nu}\,, \tag{1.2}$$

where:

- Q are quark fields,
- $\not{\mathcal{D}} = \gamma^\mu \mathcal{D}_\mu$, with $\mathcal{D}_\mu$ the covariant derivative,
- γ_μ ($\mu = 0,1,2,3$) are the Dirac matrices,
- $G^a_{\mu\nu}$ is the strong field tensor: the Yang-Mills tensor .

Quarks are

$$Q = \begin{pmatrix} U \\ D \end{pmatrix} = \begin{pmatrix} u & c & t \\ d & s & b \end{pmatrix}. \tag{1.3}$$

The strong covariant derivative is defined as

$$\mathcal{D}_\mu = \partial_\mu + i\,g_s\,G^a_\mu T^a\,. \tag{1.4}$$

The Yang-Mills tensor $G^a_{\mu\nu}$ is

$$G^a_{\mu\nu} = \partial_\mu G^a_\nu - \partial_\nu G^a_\mu - g_s f_{abc} G^b_\mu G^c_\mu \,, \tag{1.5}$$

Where:

- g_s is the $SU(3)_C$ strong coupling constant,
- G^a_μ $(a = 1, \ldots, 8)$ are the eight gluon gauge fields,
- f_{abc} are the structure constants of the $SU(3)_C$ group,
- T^a are the generators of the $SU(3)_C$ group.

The discussion of QCD will not be developed further, as it is beyond the scope of this thesis.

The Electroweak Term: $\mathcal{L}_{EW}$ and $SU(2)_L \otimes U(1)_Y$

The electroweak interaction is described by the gauge group composed of the chiral group $SU(2)_L$, and the weak hypercharge group $U(1)_Y$. The $SU(2)_L \otimes U(1)_Y$ group unifies the weak and electromagnetic forces within the Standard Model.

The electroweak Lagrangian can be written as:

$$\mathcal{L}_{EW} = i\,\bar{\psi}_L \not{D}\, \psi_L + i\,\bar{\psi}_R \not{D}\, \psi_R - \frac{1}{4} W^i_{\mu\nu} W^{i\,\mu\nu} - \frac{1}{4} B_{\mu\nu} B^{\mu\nu} \,, \tag{1.6}$$

where:

- ψ are the fermionic fields,
- L(left) and R(right) indicates fermionic fields' chirality: $\psi_{L,R} = \frac{1}{2}(1 \pm \gamma_5)\psi$,
- $W^i_{\mu\nu}$ and $B_{\mu\nu}$ are the weak and electromagnetic field tensors associated with $SU(2)_L$ and $U(1)_Y$, respectively.

The fermionic fields are:

$$\psi_L = Q_L, L_L \quad \text{and} \quad \psi_R = U_R, D_R, \ell_R \,, \tag{1.7}$$

with:

$$Q_L = \begin{pmatrix} U_L \\ D_L \end{pmatrix} = \begin{pmatrix} u_L & c_L & t_L \\ d_L & s_L & b_L \end{pmatrix} \qquad y = +\frac{1}{3} \,, \tag{1.8}$$

$$L_L = \begin{pmatrix} \nu_L \\ \ell_L \end{pmatrix} = \begin{pmatrix} \nu_{e,L} & \nu_{\mu,L} & \nu_{\tau,L} \\ e_L & \mu_L & \tau_L \end{pmatrix} \qquad y = -1 \,. \tag{1.9}$$

Q_L and L_L are doublets of weak isospin, with hypercharge $y = 2(q - I_3)$, where q is the electric charge and I_3 is the third component of weak isospin.
Right-handed fermions, singlets of weak isospin, are:

$$U_R = \begin{pmatrix} u_R & c_R & t_R \end{pmatrix} \qquad y = +\frac{4}{3} \,, \tag{1.10}$$

$$D_R = \begin{pmatrix} d_R & s_R & b_R \end{pmatrix} \qquad y = -\frac{2}{3} \,, \tag{1.11}$$

$$\ell_R = \begin{pmatrix} e_R & \mu_R & \tau_R \end{pmatrix} \qquad y = -2 \,. \tag{1.12}$$

The electroweak covariant derivative is defined as

$$D_\mu = \partial_\mu + i\,\frac{g}{2}\,W_\mu^i\,\sigma^i + i\,\frac{g'}{2}\,B_\mu\,Y\,, \tag{1.13}$$

where:

- g is the $SU(2)_L$ coupling constant,
- g' is the $U(1)_Y$ coupling constant,
- W_μ^i $(i = 1, 2, 3)$ are the $SU(2)_L$ gauge fields,
- B_μ is the $U(1)_Y$ gauge field,
- σ^i are the $SU(2)_L$ generators (Pauli matrices),
- Y is the $U(1)_Y$ generator: the hypercharge.

The field tensors are given by:

$$W_{\mu\nu}^i = \partial_\mu W_\nu^i - \partial_\nu W_\mu^i - g\,\varepsilon_{ijk}\,W_\mu^j W_\nu^k\,, \tag{1.14}$$

$$B_{\mu\nu} = \partial_\mu B_\nu - \partial_\nu B_\mu, \tag{1.15}$$

where ε_{ijk} is the structure constant of $SU(2)_L$ group (Levy-Civita tensor).

The $SU(2)_L$ symmetry acts only on the left-handed fermions, while $U(1)_Y$ applies to all fermion fields according to their hypercharge.

The Higgs Term: $\mathcal{L}_{\text{Higgs}}$

The Higgs sector introduces a scalar field that is responsible for the spontaneous breaking of the electroweak symmetry, giving mass to the gauge bosons and fermions through the Higgs mechanism [8], [9].

The Higgs Lagrangian is:

$$\mathcal{L}_{\text{Higgs}} = (D_\mu\Phi)^\dagger(D^\mu\Phi) - V(\Phi), \tag{1.16}$$

where Φ is the complex scalar Higgs, a weak isospin doublet:

$$\Phi = \begin{pmatrix} \phi^+ \\ \phi^0 \end{pmatrix} \qquad y = 1\,. \tag{1.17}$$

The covariant derivative acting on the Higgs field is the one in Equation (1.13).

The Higgs potential is given by:

$$V(\Phi) = \mu^2\Phi^\dagger\Phi + \lambda(\Phi^\dagger\Phi)^2\,. \tag{1.18}$$

The potential admits a stable minimum only if $\lambda > 0$. When also $\mu^2 < 0$, the potential develops a non-trivial minimum, leading to spontaneous symmetry breaking. In this case, the Higgs field acquires a non-zero vacuum expectation value (VEV):

$$\langle\Phi\rangle = \frac{1}{\sqrt{2}}\begin{pmatrix} 0 \\ v \end{pmatrix}, \qquad \text{with} \quad v = \sqrt{-\mu^2/\lambda}. \tag{1.19}$$

In this framework, the new gauge boson fields are:

$$W_\mu^\pm = \frac{W_\mu^1 \mp W_\mu^2}{2}\,, \tag{1.20}$$
$$Z_\mu = -B_\mu \sin\left(\theta_W\right) + W_\mu^3 \cos\left(\theta_W\right)\,, \tag{1.21}$$
$$A_\mu = +B_\mu \cos\left(\theta_W\right) + W_\mu^3 \sin\left(\theta_W\right)\,. \tag{1.22}$$

Where the physics field Z_μ and A_μ are obtained by a rotation of B_μ and W_μ^3 respect the Weinberg angle $\theta_W \equiv \tan^{-1}(g'/g)$. Using these new terms in the Higgs Lagrangian, Equation (1.17), the masses can be obtained:

$$m_H = \sqrt{2\lambda v^2}\,, \tag{1.23}$$
$$m_W = \frac{1}{2} v g\,, \tag{1.24}$$
$$m_Z = \frac{1}{2} v \sqrt{g^2 + g'^2} = \frac{m_W}{\cos\left(\theta_W\right)}\,, \tag{1.25}$$
$$m_A = 0\,. \tag{1.26}$$

The Yukawa Term: $\mathcal{L}_{\text{Yukawa}}$

While the Higgs mechanism explains the origin of gauge boson masses, the fermions in the SM remain massless until Yukawa interactions are introduced. The Yukawa Lagrangian describes gauge-invariant interactions between the Higgs field and fermion fields. After electroweak symmetry breaking, these interactions give rise to fermion mass terms.

The Yukawa Lagrangian is:

$$\mathcal{L}_{\text{Yukawa}} = -\bar{Q}_L^i Y_u^{ij} \tilde{\Phi} U_R^j - \bar{Q}_L^i Y_d^{ij} \Phi D_R^j - \bar{L}_L^i Y_\ell^{ij} \Phi \ell_R^j + \text{h.c.}\,, \tag{1.27}$$

where:

- The indices i,j = 1,2,3 run over the three quark and lepton generations,
- Y_u, Y_d, and Y_e are the Yukawa coupling matrices,
- $\tilde{\Phi} = i\sigma_2 \Phi^*$ is the charge-conjugated Higgs doublet, used to couple to up-type quarks.

After spontaneous symmetry breaking, the Higgs doublet is replaced by its VEV:

$$\Phi \to \frac{1}{\sqrt{2}} \begin{pmatrix} 0 \\ v \end{pmatrix}, \qquad \tilde{\Phi} \to \frac{1}{\sqrt{2}} \begin{pmatrix} v \\ 0 \end{pmatrix}.$$

The fermion masses for up-type quarks, down-type quarks, and leptons arise from the VEV as follows:

$$m_u = \frac{v}{\sqrt{2}} Y_u, \quad m_d = \frac{v}{\sqrt{2}} Y_d, \quad m_\ell = \frac{v}{\sqrt{2}} Y_\ell. \tag{1.28}$$

1.3.2 Quark Mixing and the CKM Matrix

The Yukawa matrices are, in general, complex and non-diagonal. In the quark sector, the diagonalization of the mass matrices leads to mixing between different generations. This mixing is described by the *Cabibbo-Kobayashi-Maskawa (CKM)* matrix: a unitary matrix that introduces a source of CP violation within the quark sector.

After electroweak symmetry breaking, the Higgs field acquires a vacuum expectation value, and the Yukawa interactions generate mass terms for the fermions. The physical mass eigenstates are obtained applying a unitary transformation to the interaction eigenstates:

$$U_{L,R} \to V_u^{L,R} U_{L,R}\,, \qquad D_{L,R} \to V_d^{L,R} D_{L,R}\,, \tag{1.29}$$

such that the mass matrices become diagonal:

$$M_u^{\text{diag}} = V_u^L Y_u V_u^{R\dagger} \left(\frac{v}{\sqrt{2}}\right), \qquad M_d^{\text{diag}} = V_d^L Y_d V_d^{R\dagger} \left(\frac{v}{\sqrt{2}}\right).$$

As a consequence, the charged current part of the Lagrangian becomes:

$$\mathcal{L}_{\text{CC}} = -\frac{g}{\sqrt{2}} \bar{U}_L \gamma^\mu V_{\text{CKM}} D_L W_\mu^+ + \text{h.c.}\,, \tag{1.30}$$

where the CKM matrix is defined as

$$V_{\text{CKM}} = V_u^L V_d^{L\dagger} = \begin{pmatrix} V_{ud} & V_{us} & V_{ub} \\ V_{cd} & V_{cs} & V_{cb} \\ V_{td} & V_{ts} & V_{tb} \end{pmatrix}. \tag{1.31}$$

Each element $V_{qq'}$ quantifies the strength of the weak transition between the up-type quark q and the down-type quark q'.
Assuming N fermion generations, the CKM would be an NxN unitary matrix contains N^2 parameters. However, not all of them are physically observable: a total of $2N-1$ parameters can be eliminated via re-phasing of the N up-type and N down-type quark fields. This leaves $(N-1)^2$ physical parameters.

Among these, $\frac{1}{2}N(N-1)$ are real parameters associated with the independent rotation angles between the basis vectors. The remaining $\frac{1}{2}(N^2-3N+2)$ parameters correspond to irreducible complex phases, which are the potential sources of CP violation.

For $N=2$, corresponding to two fermion generations, only one physical parameter remains: the Cabibbo Angle [10]. For $N=3$, as in the Standard Model, the CKM matrix is described by three mixing angles and a single irreducible complex phase [11].

CKM Parametrisations

A common parametrization of the CKM matrix uses three mixing angles $\theta_{12}, \theta_{23}, \theta_{13}$ and a complex phase δ:

$$V_{\rm CKM} = \begin{pmatrix} c_{12}c_{13} & s_{12}c_{13} & s_{13}e^{-i\delta} \\ -s_{12}c_{23} - c_{12}s_{23}s_{13}e^{i\delta} & c_{12}c_{23} - s_{12}s_{23}s_{13}e^{i\delta} & s_{23}c_{13} \\ s_{12}s_{23} - c_{12}c_{23}s_{13}e^{i\delta} & -c_{12}s_{23} - s_{12}c_{23}s_{13}e^{i\delta} & c_{23}c_{13} \end{pmatrix}, \tag{1.32}$$

where $c_{ij} = \cos\theta_{ij}$ and $s_{ij} = \sin\theta_{ij}$. Their approximate numerical values are:

$$s_{12} \simeq 0.22, \quad s_{23} \simeq 0.04, \quad s_{13} \simeq 0.0037, \quad \delta \simeq 1.1\,. \tag{1.33}$$

An alternative parametrization is the Wolfenstein expansion [12], which makes use of the hierarchy in the CKM elements:

$$V_{\rm CKM} = \begin{pmatrix} 1-\frac{\lambda^2}{2} & \lambda & A\lambda^3(\rho - i\eta) \\ -\lambda & 1-\frac{\lambda^2}{2} & A\lambda^2 \\ A\lambda^3(1-\rho-i\eta) & -A\lambda^2 & 1 \end{pmatrix} + \mathcal{O}(\lambda^4)\,, \tag{1.34}$$

where $\lambda = \sin\theta_C \simeq 0.22$, and A, ρ, η are independent parameters. The connection with the standard parametrisation is given by:

$$\lambda = s_{12}, \quad A = \frac{s_{23}}{\lambda^2}, \quad \rho + i\eta = \frac{s_{13}e^{i\delta}}{A\lambda^3} = V_{ub}^*\,. \tag{1.35}$$

It is convenient to define:

$$\bar\rho = \rho(1-\frac{\lambda^2}{2})\,, \qquad \bar\eta = \eta(1-\frac{\lambda^2}{2})\,,$$

leading to the phase convention:

$$\bar\rho + i\bar\eta = -\frac{V_{ud}V_{ub}^*}{V_{cd}V_{cb}^*}. \tag{1.36}$$

The current best-fit values for the Wolfenstein parameters are:

$$A \simeq 0.811, \quad \lambda \simeq 0.23, \quad \bar\rho \simeq 0.17, \quad \bar\eta \simeq 0.38\,. \tag{1.37}$$

From the structure of the CKM matrix, it is clear that transitions involving diagonal elements occur with the highest probability. Such transitions are known as *Cabibbo-Favoured* (CF). Transitions suppressed by λ are termed *Cabibbo-Suppressed* (CS), while those proportional to λ^2 or λ^3 are referred to as *Doubly Cabibbo-Suppressed* (DCS). This hierarchy is illustrated in Figure 1.2.

The Unitarity Triangle

Being unitary by construction, the CKM matrix satisfies the condition:

$$V_{\rm CKM}V_{\rm CKM}^\dagger = \mathbb{1}.$$

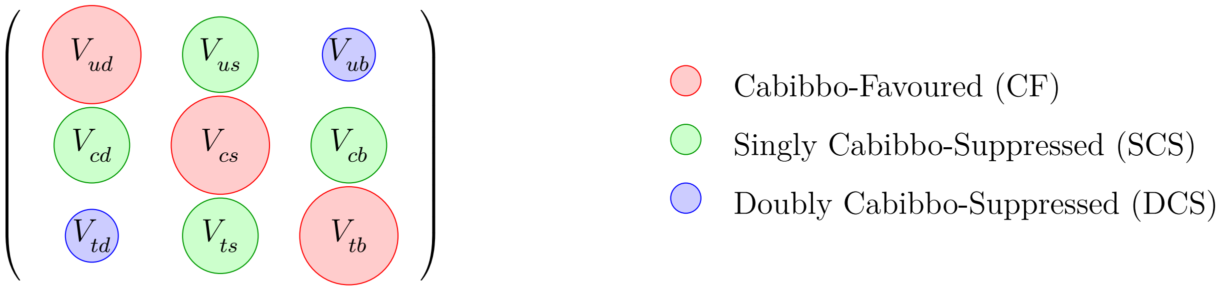

Figure 1.2: Schematic representation of CKM hierarchy. Dimensions are not to scale.

Among the unitarity conditions, six are off-diagonal orthogonality relations, each one corresponding to the vanishing sum of three complex terms:

$$V_{ud}V^*_{us}+V_{cd}V^*_{cs}+V_{td}V^*_{ts}=0 \tag{1.38a}$$
$$V_{ud}V^*_{ub}+V_{cd}V^*_{cb}+V_{td}V^*_{tb}=0 \tag{1.38b}$$
$$V_{us}V^*_{ub}+V_{cs}V^*_{cb}+V_{ts}V^*_{tb}=0 \tag{1.38c}$$

$$V_{ud}V^*_{td}+V_{us}V^*_{ts}+V_{ub}V^*_{tb}=0 \tag{1.38d}$$
$$V_{ud}V^*_{cd}+V_{us}V^*_{cs}+V_{ub}V^*_{cb}=0 \tag{1.38e}$$
$$V_{cd}V^*_{td}+V_{cs}V^*_{ts}+V_{cb}V^*_{tb}=0 \tag{1.38f}$$

These relations can be visualized as triangles in the complex plane: the *unitarity triangles*.

One of the most studied is the relation involving the first and third columns of the CKM matrix, represented in Equation (1.38b), which is particularly relevant due to the comparable magnitude of the three terms involved, of order $\mathcal{O}(\lambda^3)$. Rescaling the triangle by dividing each term by $V_{cd}V^*_{cb}$, one obtains:

$$\frac{V_{ud}V^*_{ub}}{V_{cd}V^*_{cb}}+1+\frac{V_{td}V^*_{tb}}{V_{cd}V^*_{cb}}=0\,, \tag{1.39}$$

which defines a triangle in the $(\bar{\rho},\bar{\eta})$ plane as in Figure 1.3.

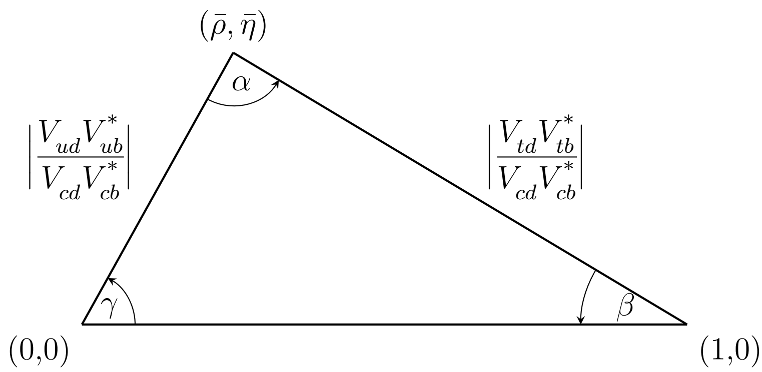

Figure 1.3: Unitarity triangle in the $(\bar{\rho},\eta)$ plane.

The angles of the unitarity triangle are defined as:

$$\alpha = \arg\left(-\frac{V_{td}V_{tb}^*}{V_{ud}V_{ub}^*}\right), \quad \beta = \arg\left(-\frac{V_{cd}V_{cb}^*}{V_{td}V_{tb}^*}\right), \quad \gamma = \arg\left(-\frac{V_{ud}V_{ub}^*}{V_{cd}V_{cb}^*}\right). \tag{1.40}$$

It can be demonstrated that the area of any unitarity triangle is identically $\frac{|J|}{2}$, where J is the *Jarlskog invariant* [13], defined:

$$J = \mathrm{Im}\left[V_{ij}V_{kl}V_{il}^*V_{kj}^*\right], \tag{1.41}$$

where (i,k) are the rows and (j,l) are the columns of the CKM, and indices are not summed. As can be seen from the definition of J, the CP violation does not depend on the specific unitarity triangle chosen.

To first approximation, in the Wolfenstein parametrization, $J \approx \lambda^6 A^2 \eta$. Therefore, CP violation occurs only if $J \neq 0$. The current best estimate is

$$J = (3.12^{+0.13}_{-0.12}) \times 10^{-5}.$$

From a geometrical point of view, CP violation occurs if the unitarity triangles do not degenerate into a straight line.

The triangle for the charm sector is in Equation (1.38e) and is represented in Figure 1.4.

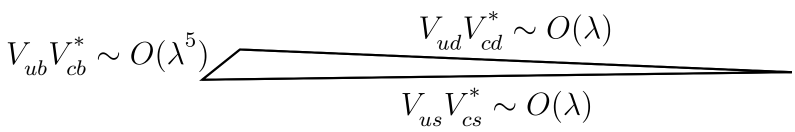

Figure 1.4: Schematic representation of the charm unitarity triangle. Sides are not to scale.

1.4 Symmetries and Neutral Mesons Mixing

In the Standard Model, the strong and electromagnetic interactions are empirically invariant under the discrete symmetries of charge conjugation, parity, and time reversal [14]:

- **Charge Conjugation (C)** transforms a particle into its corresponding antiparticle, changing sign to all internal quantum numbers such as electric charge, colour charge, flavour, baryon number, and lepton number.

- **Parity (P)** inverts all spatial coordinates: $\vec{x} \to -\vec{x}$, reflecting the system like a three-dimensional mirror. Under a parity transformation, vector and pseudo-scalar quantities change sign, while pseudo-vectors and scalars remain unchanged.

- **Time Reversal (T)** inverts the sign of the time coordinate: $t \to -t$, effectively exchanging the initial and final states of a process. This transformation reverses the momenta and angular momenta of particles.

Among the fundamental interactions, only the weak interaction violates individually all these symmetries. Nevertheless, the combined CPT symmetry remains conserved. This invariance is guaranteed by the CPT theorem, which states that any local, Lorentz-invariant quantum field theory must be invariant under the combined transformation of charge conjugation, parity, and time reversal [15].

Contrary to Landau's statement [16], the combined symmetry CP, which requires that the laws of nature remain invariant under the simultaneous action of charge conjugation and parity, is violated, albeit at different magnitudes depending on the system considered. CP violation was first observed in neutral K meson decays in 1967 [17]. Today, CPV has also been measured in the mixing systems of K, B [18–23] and D [24] mesons. This makes a detailed discussion of neutral meson mixing particularly relevant.

1.4.1 Mixing of Neutral Mesons

Neutral mesons such as $K^0-\bar{K}^0$, $B^0-\bar{B}^0$, $B_s^0-\bar{B}_s^0$, and $D^0-\bar{D}^0$ represent unique hadronic systems in which the flavour (interaction) eigenstates differ from the mass eigenstates. These mesons, when produced at time $t = 0$ as flavour eigenstates, evolve in time and oscillate between their particle and antiparticle states. Then, they decay as flavour eigenstate. This phenomenon is known as *mixing*.

In the following, we present the formalism that describes this process, focusing on $D^0-\bar{D}^0$ system. The approach is general and can be applied to the other neutral meson systems.

A generic state, initially (at t = 0) described as superposition of D^0 and $\bar{D}^0$

$$|\psi(0)\rangle = a(0)\left|D^0\right\rangle + b(0)\left|\bar{D}^0\right\rangle , \tag{1.42}$$

will evolve with as a superposition of states

$$|\psi(t)\rangle = a(t)\left|D^0\right\rangle + b(t)\left|\bar{D}^0\right\rangle + c_1(t)\left|f_1\right\rangle + c_2(t)\left|f_2\right\rangle + \dots . \tag{1.43}$$

To study the oscillation phenomenon, we adopt a simplified formalism based on the following phenomenological assumptions:

1) We restrict the analysis to the two-dimensional subspace

$$|\Psi(t)\rangle = a(t)\left|D^0\right\rangle + b(t)\left|\bar{D}^0\right\rangle .$$

2) We apply the Wigner–Weisskopf approximation [25], which assumes that the relevant interactions occur at time scales much longer than those typical of strong and electromagnetic interactions. Under this assumption, the weak interaction largely determines the system's time evolution, and the effects of the other interactions can be treated as a perturbation.

Then, the evolution of the system is described by Schrödinger's equation

$$i\partial_t |\psi(t)\rangle = i\partial_t \begin{pmatrix} D^0(t) \\ \bar{D}^0(t) \end{pmatrix} = \mathcal{H}_{eff} \begin{pmatrix} D^0(t) \\ \bar{D}^0(t) \end{pmatrix}, \tag{1.44}$$

where $\mathcal{H}_{eff}$ is the 2×2 effective Hamiltonian, which is not diagonal. Still, we can write it as a combination of two Hermitian matrices

$$\mathcal{H}_{eff} = \mathbf{M} - \frac{i}{2}\mathbf{\Gamma} \tag{1.45}$$

$$\mathbf{M} = \begin{pmatrix} M_{11} & M_{12} \\ M_{12}^* & M_{22} \end{pmatrix} \quad \mathbf{\Gamma} = \begin{pmatrix} \Gamma_{11} & \Gamma_{12} \\ \Gamma_{12}^* & \Gamma_{22} \end{pmatrix} \tag{1.46}$$

The diagonal elements of the effective Hamiltonian $\mathcal{H}_{\text{eff}} = \mathbf{M} - i\mathbf{\Gamma}/2$ correspond to flavour-conserving transitions, such as $D^0 \to D^0$ and $\bar{D}^0 \to \bar{D}^0$, while the off-diagonal elements are associated with flavour-changing processes like $D^0 \leftrightarrow \bar{D}^0$.
If we impose invariance under discrete symmetries, we can obtain constraints on the elements of the effective Hamiltonian $\mathcal{H}_{\text{eff}}$ [26]:

- **CPT symmetry** implies that $M_{11} = M_{22}$ and $\Gamma_{11} = \Gamma_{22}$.
- **CP symmetry** implies that the ratio Γ_{12}/M_{12} is real, or $\mathrm{Im}\left(\frac{\Gamma_{12}}{M_{12}}\right) = 0$.
- **T symmetry** implies $M_{12} = M_{21}^*$ and $\Gamma_{12} = \Gamma_{21}^*$. Together with the Hermiticity of the Hamiltonian, this leads to the conclusion that, if time-reversal symmetry is conserved, both M and Γ are symmetric matrices with real diagonal elements.

Assuming CPT conservation, we can diagonalize $\mathcal{H}_{\text{eff}}$ and introduce normalized coefficients such that $|p|^2 + |q|^2 = 1$. Then, the mass eigenstates are given by:

$$\begin{cases} \left|D_L\right\rangle = p\left|D^0\right\rangle + q\left|\bar{D}^0\right\rangle, \\ \left|D_H\right\rangle = p\left|D^0\right\rangle - q\left|\bar{D}^0\right\rangle. \end{cases} \tag{1.47}$$

These eigenstates, are also referred to as D_{Light} and D_{Heavy}, and possess well-defined masses and decay widths. We can express the ratio

$$\frac{q}{p} = \pm\sqrt{\frac{M_{12}^* - \frac{i}{2}\Gamma_{12}^*}{M_{12} - \frac{i}{2}\Gamma_{12}}}, \tag{1.48}$$

where in our convention we will assume the sign plus. At this point, we can express the eigenvalues of the mass matrix in terms of the parameters q and p:

$$\lambda_{L,H} = M_{11} - \frac{i}{2}\Gamma_{11} \pm \frac{q}{p}\left(M_{12} - \frac{i}{2}\Gamma_{12}\right), \tag{1.49}$$

where λ_L and λ_H correspond to the eigenvalues of the light and heavy mass eigenstates, respectively. The physical time-dependent states $\left|D^0(t)\right\rangle$ and $\left|\bar{D}^0(t)\right\rangle$ can then be written as:

$$\begin{cases} \left|D^0(t)\right\rangle = \frac{1}{2p}\left[\left|D_L(t)\right\rangle + \left|D_H(t)\right\rangle\right] , \\ \left|\bar{D}^0(t)\right\rangle = \frac{1}{2q}\left[\left|D_L(t)\right\rangle - \left|D_H(t)\right\rangle\right] . \end{cases} \tag{1.50}$$

By substituting the exponential time evolution of the mass eigenstates $\left|D_{L,H}(t)\right\rangle = e^{-i\lambda_{L,H}t}\left|D_{L,H}\right\rangle$, inverting the Equation 1.47 and defining the functions:

$$g_\pm(t) = \frac{1}{2}\left(e^{-i\lambda_L t} \pm e^{-i\lambda_H t}\right) , \tag{1.51}$$

we obtain an expression of the physical states in terms of the interaction states:

$$\left|D^0(t)\right\rangle = g_+(t)\left|D^0\right\rangle + \frac{q}{p}g_-(t)\left|\bar{D}^0\right\rangle , \tag{1.52}$$

$$\left|\bar{D}^0(t)\right\rangle = g_+(t)\left|\bar{D}^0\right\rangle + \frac{p}{q}g_-(t)\left|D^0\right\rangle , \tag{1.53}$$

where $\left|D^0(t)\right\rangle$ is the state of a particle that is a D^0 at $t = 0$. It's useful to define mass and width differences:

$$\Delta m \equiv m_H - m_L = -2\,\mathrm{Re}\left[\frac{q}{p}\left(M_{12} - \frac{i}{2}\Gamma_{12}\right)\right] , \tag{1.54}$$

$$\Delta\Gamma \equiv \Gamma_H - \Gamma_L = 4\,\mathrm{Im}\left[\frac{q}{p}\left(M_{12} - \frac{i}{2}\Gamma_{12}\right)\right] , \tag{1.55}$$

where $\Delta\Gamma$ denotes the difference in the decay widths (i.e. inverse lifetimes) of the two mass eigenstates, and Δm is the mass difference that governs the oscillation frequency.

In the literature the following parameters are also used:

$$x \equiv \frac{m_H - m_L}{\Gamma} , \qquad y \equiv \frac{\Gamma_H - \Gamma_L}{2\Gamma} , \tag{1.56}$$

where $\Gamma = \dfrac{\Gamma_H + \Gamma_L}{2}$.

The probability to obtain a flavour-defined state (D^0 or $\bar{D}^0$) at a certain time t, from an initial state of the same flavour, is proportional to $\left|\left\langle D^0 \middle| D^0(t)\right\rangle\right|^2$. An example of leading order diagrams of oscillation is in Figure 1.5. The probability is computed using the Equations 1.52,

$$\mathcal{P}(D^0(t) \to D^0) = \mathcal{P}(\bar{D}^0(t) \to \bar{D}^0) \propto \left|g_+(t)\right|^2 . \tag{1.57}$$

Analogously, the probability of mixing is:

$$\mathcal{P}(D^0(t) \to \bar{D}^0) \propto \left|\frac{q}{p}\right| \left|g_-(t)\right|^2 , \tag{1.58a}$$

$$\mathcal{P}(\bar{D}^0(t) \to D^0) \propto \left|\frac{p}{q}\right| \left|g_-(t)\right|^2 . \tag{1.58b}$$

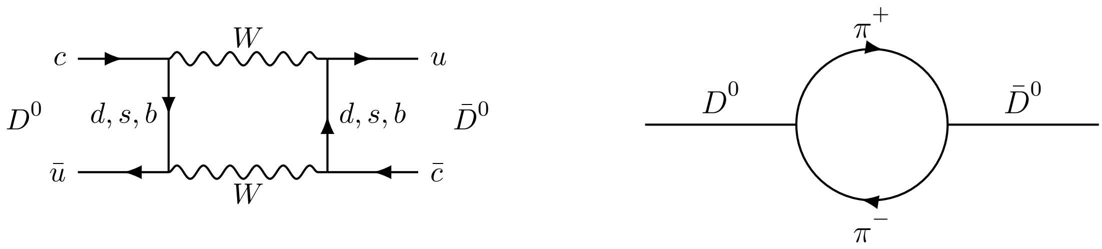

Figure 1.5: Example of leaning order diagram of oscillation $D^0 - \bar{D}^0$. Short-range contribution (left) and long-range contribution, through intermediate hadronic states (right).

Instead, if CP is conserved (or T), $|p/q| = 1$ and

$$\mathcal{P}(D^0(t) \to D^0) = \tfrac{1}{2}e^{-\Gamma t}\left(\cosh\left(\frac{\Delta\Gamma}{2}t\right) + \cos\left(\Delta m\ t\right)\right) , \tag{1.59a}$$

$$\mathcal{P}(D^0(t) \to \bar{D}^0) = \tfrac{1}{2}e^{-\Gamma t}\left(\cosh\left(\frac{\Delta\Gamma}{2}t\right) - \cos\left(\Delta m\ t\right)\right) . \tag{1.59b}$$

In Figure 1.6, the transition probabilities for all four mixing systems of neutral mesons are plotted in the case of flavour changing, no flavour changing, and the exponential decay.

1.5 CP Violation in the Quark Sector

Within the Standard Model, due to the irreducible phase of the CKM matrix, several parameters related to CP violation in the quark sector, such as the Jarlskog invariant and the unitarity triangles discussed in Section 1.3.2.

Experimentally, in the case of neutral meson systems, CP violation can occur through three distinct mechanisms:

- **CP violation in the Decay**, occurring in the decay process;
- **CP violation in the Mixing**, arising in the phenomenon of mesons mixing;
- **CP violation in the Interference** between decay with and without mixing.

We now proceed to discuss each of these mechanisms in detail.

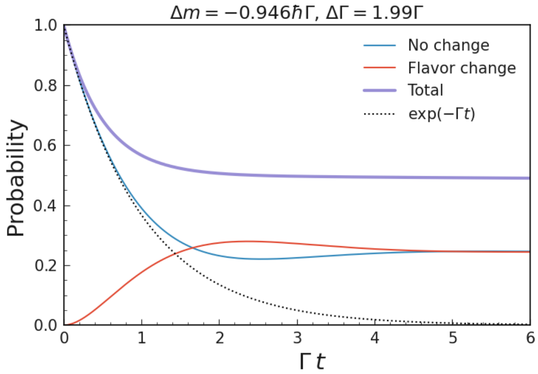

(a) $K^0 - \bar{K}^0$ system.

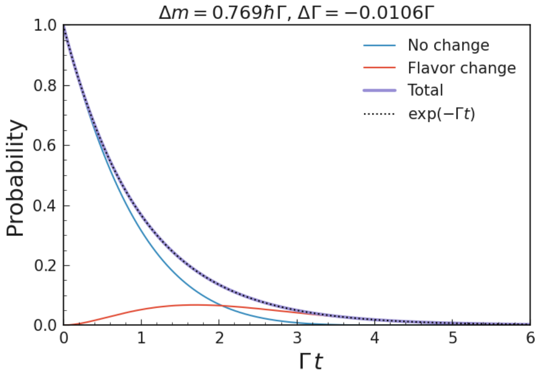

(b) $B^0 - \bar{B}^0$ system.

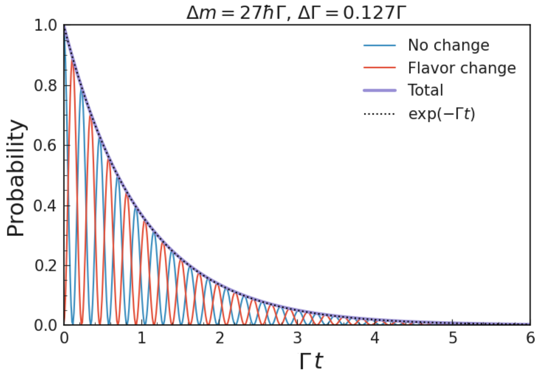

(c) $B_s^0 - \bar{B}_s^0$ system.

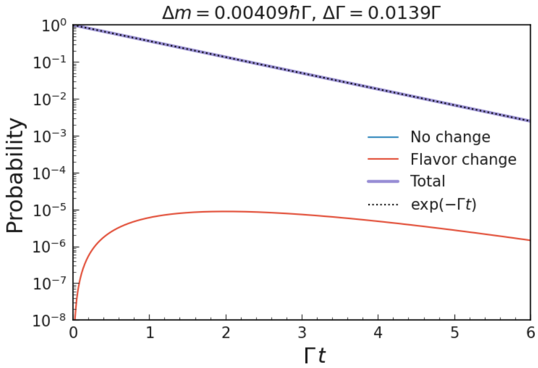

(d) $D^0 - \bar{D}^0$ system.

Figure 1.6: Plot of the oscillation probability of neutral mesons in the four mixing systems, evaluated for fixed values of Δm and $\Delta\Gamma$. The red and blue curves represent, respectively, the transition probabilities with and without flavour change. The purple curve corresponds to their sum, while the dashed line indicates the purely exponential decay that would be expected in the absence of mixing.

1.5.1 CP Violation in the Decay

In the decay of a neutral or a charged D meson, CPV occurs when the probability of transition of the decay A is different from the CP-conjugate $\bar{A}$,

$$|A| \neq |\bar{A}| .$$

To observe this type of CPV, the total decay amplitude must have at least two terms with different strong phases (CP even) and weak phases (CP odd) that interfere. We define the decay amplitudes of a D and a $\bar{D}$ meson into a specific final state and its CP-conjugate, through the weak interaction Hamiltonian:

$$A = \langle f | H_w | D \rangle \,, \qquad \bar{A} = \left\langle \bar{f} \middle| H_w \middle| \bar{D} \right\rangle . \tag{1.60}$$

When the decay can occurs through two possible diagrams, the total decay amplitudes can then be written as:

$$A = |A_1| e^{i\delta_1} e^{i\phi_1} + |A_2| e^{i\delta_2} e^{i\phi_2} \,, \qquad \bar{A} = |A_1| e^{i\delta_1} e^{-i\phi_1} + |A_2| e^{i\delta_2} e^{-i\phi_2} \,, \tag{1.61}$$

where δ and ϕ denote the strong and weak phases, respectively.

We obtain:

$$|A|^2 - |\bar{A}|^2 = 4|A_1||A_2| \sin\left(\delta_1 - \delta_2\right) \sin\left(\phi_1 - \phi_2\right), \tag{1.62}$$

which is directly connected with an observable sensitive to these phenomena, and the one discussed in this thesis, the *CP Asimmetry*:

$$\mathcal{A}_{\mathrm{CP}} = \frac{\Gamma(D^0 \to f) - \Gamma(\bar{D}^0 \to \bar{f})}{\Gamma(D^0 \to f) + \Gamma(\bar{D}^0 \to \bar{f})}. \tag{1.63}$$

1.5.2 CP Violation in the Mixing

This kind of CPV arise when $\left|D_L\right\rangle$ and $\left|D_H\right\rangle$ aren't orthogonal. From Equation (1.47):

$$\left|\frac{p}{q}\right| \neq 1. \tag{1.64}$$

In the presence of CP violation, the transition probability for the physical time-dependent eigenstates to oscillate as $D^0(t) \to \bar{D}^0(t+\Delta t)$ differs from $\bar{D}^0(t) \to D^0(t+\Delta t)$. The physical eigenstates are defined in Equations (1.52) and (1.53), and the probability to mix in Equation (1.58).

To experimentally access CPV in mixing, we proceed to consider a decay in a final state f. We can assume a flavour-changing decay through a weak Hamiltonian, so the amplitudes are defined as:

$$A_f = A(D^0 \to f) = \langle f| H_w \left|D^0\right\rangle, \quad A_{\bar{f}} = A(D^0 \to \bar{f}) = \left\langle \bar{f}\right| H_w \left|D^0\right\rangle, \tag{1.65}$$

$$\bar{A}_f = A(\bar{D}^0 \to f) = \langle f| H_w \left|\bar{D}^0\right\rangle, \quad \bar{A}_{\bar{f}} = A(\bar{D}^0 \to \bar{f}) = \left\langle \bar{f}\right| H_w \left|\bar{D}^0\right\rangle, \tag{1.66}$$

and consider decay rates

$$\frac{d}{dt}\Gamma(D^0(t) \to f) \propto \left|\langle f| H_w \left|D^0(t)\right\rangle\right|^2, \qquad \frac{d}{dt}\Gamma(\bar{D}^0(t) \to \bar{f}) \propto \left|\left\langle \bar{f}\right| H_w \left|\bar{D}^0\right\rangle\right|^2, \tag{1.67}$$

we obtain

$$\frac{d}{dt}\Gamma(D^0(t) \to f) \propto \left|g_+(t)\ \langle f| H_w \left|D^0\right\rangle + \frac{q}{p}\ g_-(t)\ \langle f| H_w \left|\bar{D}^0\right\rangle\right|^2 \tag{1.68a}$$

$$= \left|g_+(t)\ A_f + \frac{q}{p}\ g_-(t)\ \bar{A}_f\right|^2,$$

$$\frac{d}{dt}\Gamma(\bar{D}^0(t) \to \bar{f}) \propto \left|g_+(t)\ \left\langle \bar{f}\right| H_w \left|\bar{D}^0\right\rangle + \frac{p}{q}\ g_-(t)\ \left\langle \bar{f}\right| H_w \left|D^0\right\rangle\right|^2 \tag{1.68b}$$

$$= \left|g_+(t)\ \bar{A}_{\bar{f}} + \frac{p}{q}\ g_-(t)\ A_{\bar{f}}\right|^2.$$

An important channel to be sensitive to CPV in mixing is the semi-leptonic decays, because the charge of the lepton identifies the flavour of the decayed meson. Only the *wrong-sign* decays are considered, since they can occur solely through mixing.

The experimental observable is $\mathcal{A}_{SL}$:

$$\mathcal{A}_{SL}(t) = \frac{\frac{d}{dt}\Gamma(D^0(t)\to l^+X^-) - \frac{d}{dt}\Gamma(\bar{D}^0(t)\to l^-X^+)}{\frac{d}{dt}\Gamma(D^0(t)\to l^+X^-) + \frac{d}{dt}\Gamma(\bar{D}^0(t)\to l^-X^+)} = \frac{1-\left|\frac{p}{q}\right|^4}{1+\left|\frac{p}{q}\right|^4}\,. \tag{1.69}$$

1.5.3 CP Violation in the Interference

The third CP violation mechanism arises when both D^0 and $\bar{D}^0$ can decay into the same final state $f = \bar{f}$. In this case, the final state can be reached either through a direct decay of the meson (potentially exhibiting direct CP violation), or via mixing followed by a decay of the CP-conjugate meson.

In this case, the decay rates can be expressed as:

$$\frac{d}{dt}\Gamma(D^0(t)\to f) \propto \left|A_f\right|^2 \; \left|g_+(t) + \lambda_f\; g_-(t)\right|^2, \tag{1.70a}$$

$$\frac{d}{dt}\Gamma(\bar{D}^0(t)\to \bar{f}) \propto \left|\bar{A}_{\bar{f}}\right|^2 \; \left|g_+(t) + \frac{1}{\lambda_{\bar{f}}}\; g_-(t)\right|^2, \tag{1.70b}$$

where

$$\lambda_f \equiv \frac{q}{p}\frac{\bar{A}_f}{A_f}\,, \qquad \lambda_{\bar{f}} \equiv \frac{q}{p}\frac{\bar{A}_{\bar{f}}}{A_{\bar{f}}}. \tag{1.71}$$

CP violation occurs when:

$$\arg[\lambda_f] + \arg[\lambda_{\bar{f}}] \neq 0\,. \tag{1.72}$$

However, if f is a CP eigenstate, this condition simplifies to:

$$\mathrm{Im}[\lambda_f] \neq 0\,.$$

CP violation in the interference can also occur when neither decay nor mixing CP violation is present: that is, when $|q/p| = 1$ **and/or** $\left|\bar{A}_f/A_f\right| = 1$.

Chapter 2

$D^0 \to \pi^+\pi^-\pi^0$ Dalitz Plot

The chapter begins by discussing the motivation for investigating CP violation in the selected decay channel. It introduces the Dalitz plot, tracing its development from the original formulation to modern applications. Then, results from a theoretical paper providing a prediction of SM CP violation are presented. These results will be used in the next chapter to assess the statistical significance of $\mathcal{A}_{\mathrm{CP}}$. Finally, the Laura++ package used to produce Dalitz plot distributions is briefly described.

2.1 CP Violation in the $D^0 \to \pi^+\pi^-\pi^0$ Decay

The study of CP violation in the charm sector represents a particularly compelling research direction in the search for physics beyond the Standard Model. Within the SM framework, CPV in decays of charmed mesons is expected to be extremely small, typically of the order of 10^{-3} or less in most channels. So, any observation of CP asymmetries significantly larger than the SM predictions would provide an unambiguous indication of contributions from new physics.

Additional motivation arises from the phenomenon of D^0–$\bar{D}^0$ mixing, whose dynamics within the SM are subject to large theoretical uncertainties due to non-perturbative QCD effects. At the same time, since the charm quark belongs to the up-type family, its study offers a unique probe of CP violation in a sector that remains comparatively less explored than the strange and beauty systems.

In this context, the chosen decay channel investigated in this thesis is $D^0 \to \pi^+\pi^-\pi^0$. This decay mode is of particular interest for several reasons. First, the $c \to ud\bar{d}$ transition is a Singly Cabibbo-Suppressed (SCS) decay, a class of decays where CPV is expected to be larger. Second, the decay proceeds predominantly via intermediate resonant states of two pions, resulting in multiple interfering amplitudes, each of which can potentially exhibit CP violation. Moreover, the final state is common to both D^0 and $\bar{D}^0$, making it also sensitive to CP violation in the interference between decays with and without mixing. Finally, the presence of neutral particles in the final state renders this experimentally challenging, but it is perfectly feasible at Belle II.

2.2 The Dalitz Plot

The Dalitz plot (DP) was introduced in 1953 by R.H. Dalitz as a graphical tool to represent the kinematically allowed phase space of three-body decays of the form $P \to d_1 + d_2 + d_3$. For the first time it was applied to study the decay of the τ meson–later reinterpreted as the charged kaon–into three pions [27, 28]. In this early, non-relativistic formulation, the accessible phase space was represented as a circle inscribed within an equilateral triangle, as shown in Figure 2.1. The radius of the circumference is proportional to the total available kinetic energy in the decay, $Q = T_1 + T_2 + T_3$, with $T_i = E_i - m_i$ denoting the kinetic energy of each particle.

In this picture, the center represents the configuration in which all particles have the same kinetic energy. A generic configuration, indicated by a point P, corresponds instead to different values of T_i. These are mapped onto the plane using the coordinates

$$x = \sqrt{3}(T_1 - T_2), \qquad y = 2T_3 - T_1 - T_2\,,$$

where the distances from the sides of the triangle reflect the kinetic-energy distribution among the three particles.

In the $K^+ \to 3\pi$ decay, the phase-space representation is a perfect circle because the three final-state particles are pions of equal mass, resulting in a completely symmetric kinematic configuration.

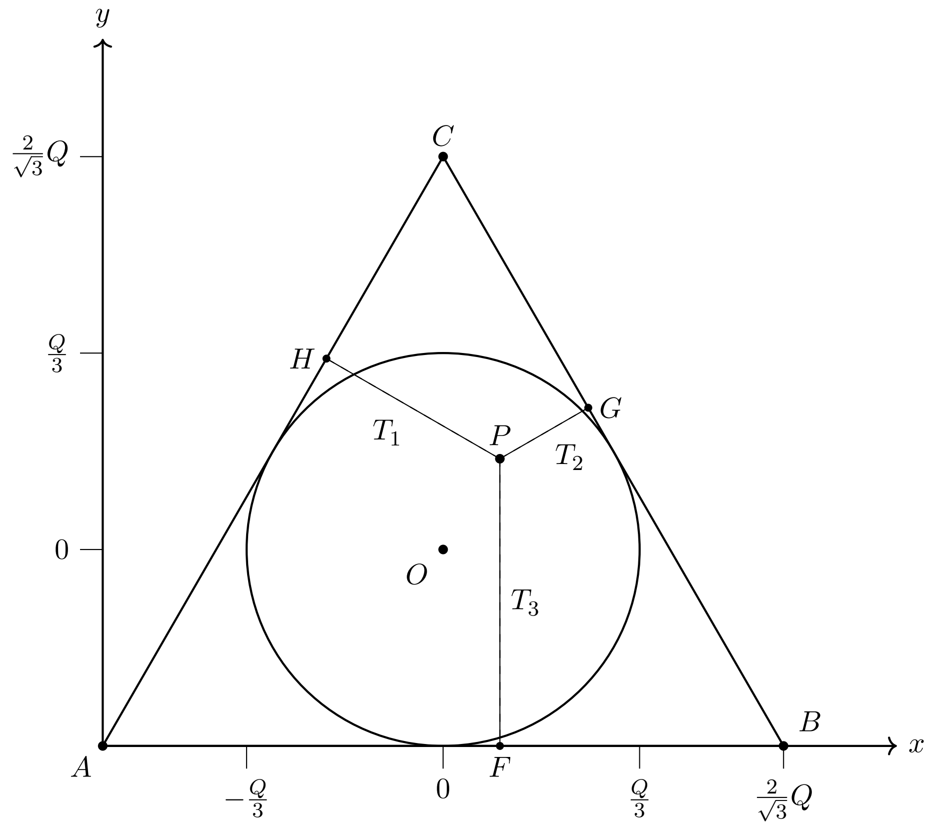

Figure 2.1: Scheme of the original Dalitz Plot of the decay $K^+ \to 3\pi$.

2.2.1 The Modern Dalitz Plot

Nowadays, is used the relativistic formulation of the Dalitz plot, where axes are defined by the squared invariant masses of the final-state particle pairs m_{12}^2 and m_{13}^2.

In the following discussion, we restrict our attention to only decays into three scalar particles. In this case, only two variables are sufficient to completely describe the three-body phase space. Starting from the twelve degrees of freedom associated with the three four-momenta of the final-state particles, a series of kinematic constraints reduces the system to only two independent variables. These constraints are: four-momentum conservation, the fixed values of the particle masses, and the three Euler angles describing the orientation of the decay in space, as summarized in Table 2.1.

3 four-vectors	+12
Energy conservation	-1
Momentum conservation	-3
3 masses	-3
3 Euler angles	-3
Total degrees of freedom	+2

Table 2.1: Number of degrees of freedom in a three-body decay.

The squared invariant masses of two particle pairs are defined as

$$m_{ij}^2 = (P_i^\mu + P_j^\mu)^2 \,,$$

which, in the rest frame of the parent particle of mass M, can be written as:

$$m_{12}^2 = (E_1 + E_2)^2 - (\vec{p}_1 + \vec{p}_2)^2 = M^2 - 2ME_3 + m_3^2 \,, \tag{2.1}$$
$$m_{13}^2 = (E_1 + E_3)^2 - (\vec{p}_1 + \vec{p}_3)^2 = M^2 - 2ME_2 + m_2^2 \,, \tag{2.2}$$
$$m_{23}^2 = (E_2 + E_3)^2 - (\vec{p}_2 + \vec{p}_3)^2 = M^2 - 2ME_1 + m_1^2 \,. \tag{2.3}$$

In this representation, the physically accessible phase space is entirely enclosed within a well-defined kinematic boundary of the Dalitz plot. The kinematics asymptotes are due to limiting configurations imposed by energy–momentum conservation: when a particle is produced at rest in the parent rest frame while the other two are emitted back-to-back, or two particles are produced collinearly and the third recoils with opposite momentum. These constraints translate into the following kinematic limits:

$$(m_1 + m_2)^2 \leq m_{12}^2 \leq (M - m_3)^2 \,, \tag{2.4}$$
$$(m_1 + m_3)^2 \leq m_{13}^2 \leq (M - m_2)^2 \,, \tag{2.5}$$
$$(m_2 + m_3)^2 \leq m_{23}^2 \leq (M - m_1)^2 \,, \tag{2.6}$$

and are illustrated schematically in Figure 2.2.

The shape of the Dalitz plot strongly depends on the amount of kinetic energy released in the decay, $Q = M - m_1 - m_2 - m_3$. When the available energy Q is small

($M \simeq m_1 + m_2 + m_3$), the system is close to the non-relativistic regime and the allowed phase space tends to assume an approximately circular shape. Conversely, in the ultra-relativistic limit ($E_i \gg m_i$), the boundaries of the Dalitz plot converge towards a triangular region.

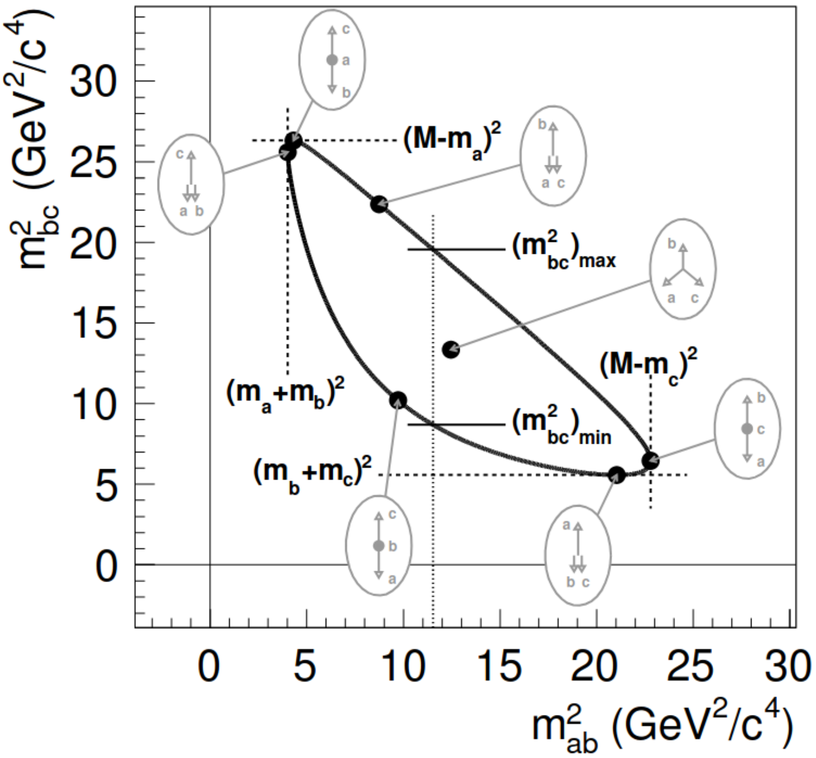

Figure 2.2: Visual scheme of a relativistic Dalitz plot. In this example, the $B^0 \to \pi^- D^0 K^+$ phase space is shown; with $a = \pi^-$, $b = D^0$, and $c = K^+$ [29].

2.2.2 Resonances in the DP

The entire phase space density of a three-body decay can be described by the two variables m^2_{13} and m^2_{23}:

$$\mathrm{d}\Gamma = \frac{1}{(2\pi)^3}\frac{1}{32M^3}|A(m^2_{13}, m^2_{23})|^2\, \mathrm{d}m^2_{13}\, \mathrm{d}m^2_{23}\,, \tag{2.7}$$

with M the mass of the parent particle and A the invariant total amplitude that contains all the dynamics of the process. So, the Dalitz plot provides a graphical representation of the kinematic configuration, allowing the underlying dynamics of the decay to be visualized: in the case of a constant decay amplitude A, the density of events is uniformly distributed over the allowed phase space; conversely, the presence of intermediate resonant states manifests itself as localized non-uniform structures, which can be identified by eye.

A common way to parametrize the amplitude $A(m^2_{13}, m^2_{23})$ is the *isobar model* [30, 31], where the sum of N resonant and a non-resonant contributions describes the total amplitude:

$$A(m_{13}^2, m_{23}^2) = \sum_{r=1}^{N} c_r A_r(m_{13}^2, m_{23}^2) + c_{NR} A_{NR}(m_{13}^2, m_{23}^2)\,, \tag{2.8}$$

where the complex coefficients are $c_r = a_r e^{\delta_r}$. a_r give the various relative contributions, and the phases δ_r account for final state interaction. A_{NR} are the amplitudes of non-resonance states and A_r are the amplitudes of resonances, normalized in the full Dalitz Plot

$$\int\int_{DP} |A_r(m_{13}^2, m_{23}^2)|^2 \mathrm{d}m_{13}^2 \mathrm{d}m_{23}^2 = 1\,. \tag{2.9}$$

In the partial-wave decomposition the resonances decay in a specific partial wave state of the final particles, since the resonance appears in a well-defined spin [32]. In the Gottfried frame, i.e. the rest frame of the two scalar(pseudoscalar) particle system $d_1 d_3$ (see Figure 2.3), the amplitude associated with the decay of a resonance depends on a Breit-Wigner term and a Legendre polynomial:

$$A_{r\to 13} \sim A_{\mathrm{BW}}\, P_s(\cos\theta)\,, \tag{2.10}$$

where $P_s(\cos\theta)$ denotes the Legendre polynomial of order s, corresponding to the spin of the resonance, and θ is the angle between particle d_1 and particle d_3 in this reference frame. The first few orders of the Legendre polynomial are

$$P_0(\cos\theta) = 1\,, \quad P_1(\cos\theta) = \cos\theta\,, \quad P_2(\cos\theta) = \frac{1}{2}\left(3\cos^2\theta - 1\right)\,.$$

This functional dependency is directly reflected in the Dalitz plot: the locations of the zeros in the distribution of a resonance depend on its spin, and these features can be easily read from the plot itself, as we can notice in Figure 2.4.

The Breit-Wigner amplitude A_{BW} is given by

$$A_{\mathrm{BW}} = \frac{1}{m_r^2 - m_{13}^2 - i m_r \Gamma}\,, \tag{2.11}$$

where m_r is the mass of the resonance and $\Gamma = \hbar/\tau$ represents the decay width, inversely related to the lifetime τ of the resonance.

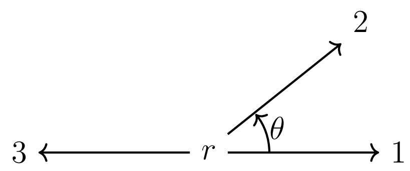

Figure 2.3: Scheme of the Gottfried frame of a resonance decay $r \to d_1 d_3$.

From the Dalitz plot, it is possible to extract further information about the properties of resonances. In particular, a resonance occurs as a sharp band, and its distribution allows for estimating its width and its mass.

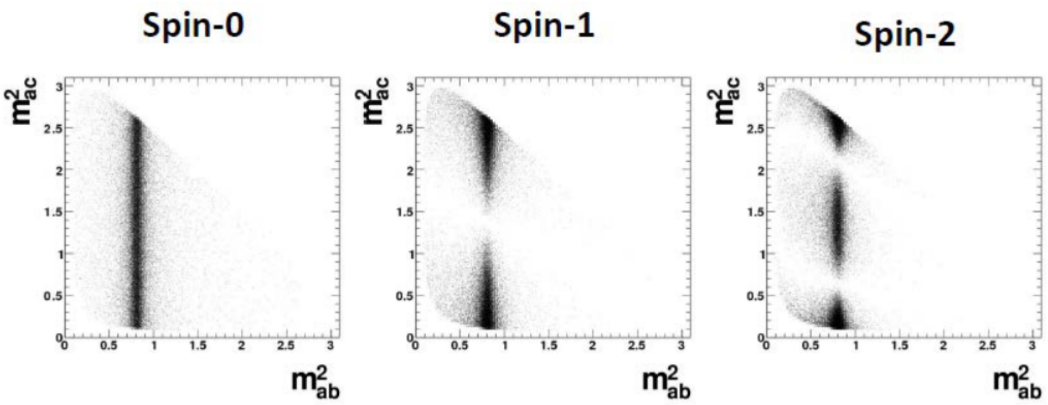

Figure 2.4: Scatter plot of resonances of particles ab ($d_1 d_3$ in our disquisition) with different spins.

2.2.3 CP Violation with the Dalitz Plot

One of the most critical applications of the Dalitz plot is the study of CP violation in three-body decays. The DP is sensitive to both strong and weak phases, whose values depend on the local position within the plot. A non-vanishing CP asymmetry can arise only in the presence of interference between at least two distinct amplitudes, with different weak and strong phases. The key aspect, which we will further develop, is that when integrating over the entire phase space, the contributions of these phases can average out, thereby diluting the measurable CP violation. Conversely, by focusing on restricted regions of the Dalitz plot, such effects can become significantly more pronounced and experimentally accessible.

When analysing three-body decays using the Dalitz plot, two complementary strategies can be employed: a *model-dependent* and a *model-independent* approach. In the model-dependent case, the interpretation of the data relies on the parametrization of the decay amplitudes. In particular, the presence of intermediate resonant states, where the decay proceeds effectively through a quasi-two-body process, makes the result sensitive to the functional form chosen to describe the resonances and to the interference patterns among them. As a consequence, studying processes of the type $r\, d_i \to d_1 d_2 d_3$ may introduce systematic uncertainties in the extraction of CP violation, since the outcome depends on the theoretical assumptions made in modeling the resonance dynamics.

In contrast, the model-independent approach is based solely on general considerations about the distributions of the final-state particles in the Dalitz plot, without relying on specific functional forms for the decay amplitudes. In this framework, the description of the partial process $P \to r\, d_i$ does not depend on the chosen parametrization of the resonance model.

An additional aspect to be addressed concerns the choice of the DP region where to search for CP violation. The definition of the region size represents a compromise between statistical precision and the ability to resolve the underlying structure of the DP. Large region sizes guarantee higher statistics and thus smaller statistical uncertainties, but may hide finer details of the distribution. Conversely, smaller regions are more sensitive to local structures in the DP, but may suffer from reduced statistics and correspondingly larger uncertainties. An analysis of the entire Dalitz Plot offers the advantage of utilizing the full available statistics, thereby reducing overall statistical errors. However, it does not allow the study of local variations in CP violation across different regions of the phase space, which is instead possible with a binned approach.

A theoretical model guides the choice of the interesting region, which will be explored in Section 2.4. However, before proceeding, I will discuss the *Laura++* package analysis tool [33].

2.3 The *Laura++* Package

To obtain a representative model of the Dalitz plot for the decay $D^0(\bar{D}^0) \to \pi^+\pi^-\pi^0$, including the two-pion resonant substructures, I used *Laura++*. It is a nearly stand-alone software package, written in *C++*, with the only external dependency being the *ROOT* framework, and provides a comprehensive framework for constructing and fitting amplitude models of three-body decays, based on the isobar formalism.

Laura++ allows the expression of the total decay amplitude as the coherent sum of resonant and non-resonant contributions, each described by well-defined dynamical functions such as relativistic Breit-Wigner line shapes or alternative parametrizations.

The package natively supports the modelling of angular distributions and the treatment of interference effects between intermediate states. Furthermore, *Laura++* provides a precise and flexible description of resonance models through adjustable parameters, such as masses, widths, and spin values, enabling an accurate simulation of the dynamical behaviour. These features make it particularly well-suited for the study of $D^0(\bar{D}^0) \to \pi^+\pi^-\pi^0$ decays, where multiple interfering resonant contributions from two-pion subsystems play a central role in shaping the Dalitz plot distribution.

Modelling Resonances

To model the decay process, *Laura++* requires, among various inputs, the specification of the parent particle and its decay products, the chosen dynamical model, and the set of parameters describing the intermediate resonances.

For each resonance, it is necessary to provide the functional form that describes its dynamics (the amplitude) — here implemented as a relativistic Breit-Wigner lineshape — together with its associated parameters. These are the complex coefficients of Equation (2.8), expressed as $c_r = \alpha\, e^{i\phi_r}$, where α is the magnitude and ϕ_r the phase of the resonance contribution. The parameters I used were taken from the fit results published by the BaBar collaboration [34], reported in Table 2.2.

It should be noted, however, that *Laura++* adopts a different phase convention: for resonances with positive charge, I applied a phase shift of $+180^\circ$ relative to the BaBar definition.

State	f_r (%)	$\sqrt{f_r}$	ϕ_r (rad)
$\rho^+(770)$	67.8	0.823	π
$\rho^0(770)$	26.2	0.511	0.28
$\rho^-(770)$	34.6	0.589	-0.035
$\rho^+(1450)$	0.11	0.033	0.59
$\rho^0(1450)$	0.30	0.055	0.17
$\rho^-(1450)$	1.79	0.134	0.28
$\rho^+(1700)$	4.1	0.202	2.84
$\rho^0(1700)$	5.0	0.224	-0.30
$\rho^-(1700)$	3.2	0.179	-0.87
$f_0(980)$	0.25	0.050	-1.03
$f_0(1370)$	0.37	0.061	2.72
$f_0(1500)$	0.39	0.062	0.21
$f_0(1710)$	0.31	0.056	0.89
$f_2(1270)$	1.32	0.115	-2.98
$\sigma(400)$	0.82	0.091	0.14
Non-Res	0.84	0.092	-0.19

Table 2.2: Fit fractions f_r, corresponding amplitudes $\sqrt{f_r}$, and phase differences ϕ_r in radians for the $D^0 \to \pi^+\pi^-\pi^0$ sample. A phase shift of +180° is applied only to positively charged resonances.

The magnitude of the complex coefficient is expressed in terms of a directly related quantity, the square root of the *fit fraction*, defined as

$$f_r = \frac{\int |c_r A_r(m_{13}^2, m_{23}^2)|^2 \, dm_{13}^2 dm_{23}^2}{\int |A(m_{13}^2, m_{23}^2)|^2 \, dm_{13}^2 dm_{23}^2} . \tag{2.12}$$

The fit fraction represents the relative contribution of a given intermediate state to the overall decay rate.

Finally, by defining the number of events for each toy pseudo-experiment and the number of those, I can generate a ROOT file with a custom total number of events in our signal channel. In Figure 2.5 I generated a total of 15×10^6 events of only D^0, corresponding to integrated luminosity of $L_{int} \simeq 2.5\,\mathrm{ab}^{-1}$ at Belle II.

In this work, the focus is restricted to the $\rho^{\pm}(770)$ resonances, following the approach discussed in Section 2.4. For this reason, it is helpful to visualize their distribution within the Dalitz plot, as illustrated in Figure 2.6.

2.4 Theoretical Prediction

In flavour physics, approximate quark symmetries such as U-spin provide a helpful framework for identifying systematic patterns in hadronic decays. U-spin symmetry treats the down and strange quarks as members of an $SU(2)$ doublet (d, s), a

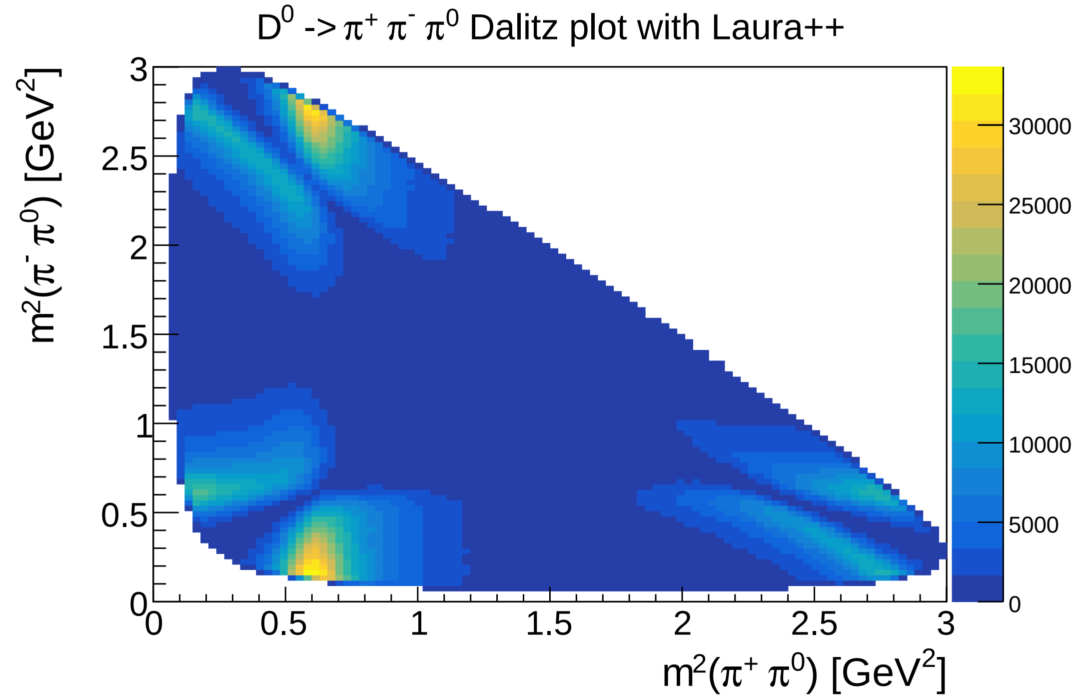

Figure 2.5: Laura++ generated Dalitz plot. 15000 events of $D^0 \to \pi^+\pi^-\pi^0$ for each experiment, for 1000 experiments. In total 15×10^6 events. 100×100 bins.

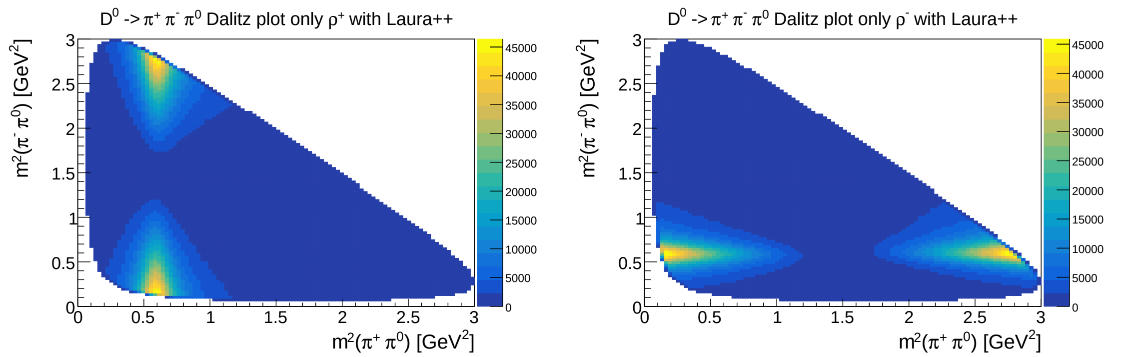

(a) Daltiz plot generated considering exclusively the $\rho^+(770)$ resonance.

(b) Daltiz plot generated considering exclusively the $\rho^-(770)$ resonance.

Figure 2.6: Laura++ generated 15×10^6 events of $D^0 \to \pi^+\pi^-\pi^0$ decay, considering exclusively two resonances. 100×100 bins.

subgroup of the larger flavour symmetry SU(3), allowing decay amplitudes to be classified according to their transformation properties under this symmetry.

Experimentally, it has been observed that in charm decays, processes preserving U-spin ($\Delta U = 0$), as described in [35], occur with significantly higher probability than those that change it ($\Delta U = 1$). This behavior, known as the $\Delta U = 0$ *rule*, indicates that weak interaction dynamics tend to enhance amplitudes conserving U-spin while suppressing those associated with U-spin–breaking transitions.

The rule has already been tested in connection with CP asymmetry in two-body decays such as $D^0 \to P^{\pm}P^{\mp}$ [36], where P denotes a pseudoscalar meson. Building on this, the study presented in Ref. [37], which forms the basis of the approach adopted in this thesis, extends the test to three-body decays. In this framework, the amplitude is parametrized as a sequence of quasi-two-body processes of the form $D^0 \to V^{\pm}P^{\mp}$, where the vector meson subsequently decays strongly via $V^{\pm} \to P^{\pm}P^0$.

For simplicity, the study focuses exclusively on the region of interference between $\rho^+(770)$ and $\rho^-(770)$ mesons, where other resonance contributions are negligible:

$$D^0 \to (\rho^+ \to \pi^+\pi^0)\pi^- \,, \quad D^0 \to (\rho^- \to \pi^-\pi^0)\pi^+ \,, \tag{2.13}$$

$$\bar{D}^0 \to (\rho^+ \to \pi^+\pi^0)\pi^- \,, \quad \bar{D}^0 \to (\rho^- \to \pi^-\pi^0)\pi^+ \,, \tag{2.14}$$

and connects this rule to CP Violation in this channel.

The model uses the effective Hamiltonian, which rules the decay in a $\Delta\mathrm{U} = 1$ and $\Delta\mathrm{U} = 0$ state:

$$H_{eff} \sim \lambda_{sd} H_{(1,0)} - \frac{\lambda_b}{2} H_{(0,0)} \,, \tag{2.15}$$

where the coefficients are the following CKM terms:

$$\lambda_{sd} \equiv \frac{V^*_{cs}V_{us} - V^*_{cd}V_{ud}}{2} \,, \quad -\frac{\lambda_b}{2} \equiv -\frac{V^*_{cb}V_{ub}}{2} = \frac{V^*_{cs}V_{us} + V^*_{cd}V_{ud}}{2} \,. \tag{2.16}$$

For this thesis, the numerical simulation shown in Figure 2.7 is employed to evaluate the measurability of the asymmetry.

The CP asymmetry shown in Figure 2.7 in this parametrisation depends on the ratio between the $\Delta U = 0$ and $\Delta U = 1$ contributions, defined as:

$$\tilde{R}^{P_iV_j} \equiv \frac{R^{P_iV_j}}{T^{P_iV_j}} \,, \text{where :} \tag{2.17}$$

$$R^{P_iV_j} = \left\langle P_i V_j \right| H_{(0,0)} \left| D^0 \right\rangle \,, \tag{2.18}$$

$$T^{P_iV_j} = \left\langle P_i V_j \right| H_{(1,0)} \left| D^0 \right\rangle \,. \tag{2.19}$$

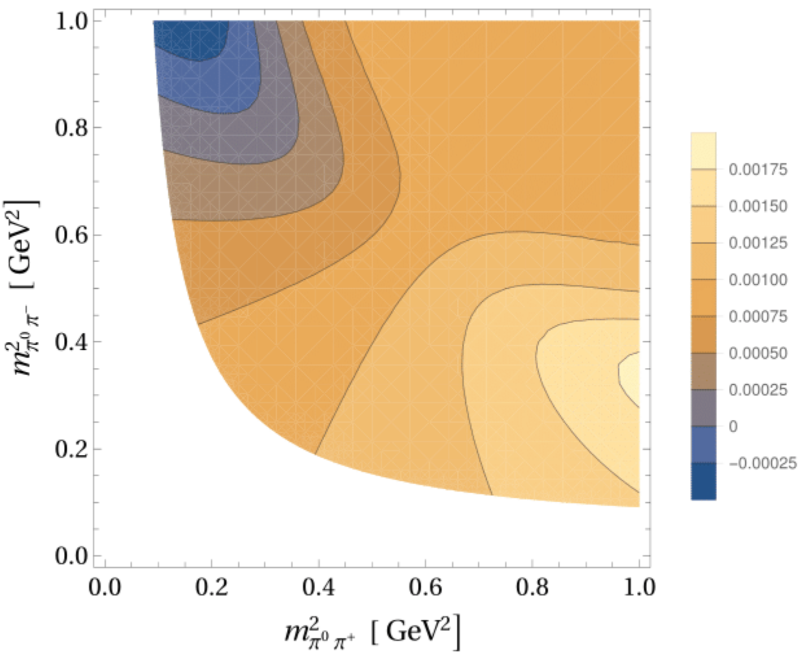

(c) $\widetilde{R}^{P_1V_2} = \frac{1}{2}\exp(i\pi/2), \quad \widetilde{R}^{P_2V_1} = \exp(i\pi/3)$

Figure 2.7: Predicted asymmetry in a reduced region of the Dalitz plot from [37].

Chapter 3

The Measurement at Belle II

The chapter opens with a discussion of the motivations behind the construction of B-factories, designed primarily to produce large samples of b-quarks, while also offering valuable opportunities for the study of charm physics. It then introduces the experimental facilities that provide the simulated data used in this work, namely the SuperKEKB accelerator and the Belle II detector. The chapter concludes with an overview of the strategies adopted by Belle II for particle reconstruction and identification, both for charged and neutral final-state particles, as well as the experimental asymmetries involved in the measurement. The chapter concludes with a discussion on the experimental asymmetries that affect the measurement.

3.1 Introduction to B Factories

In the early 1970s, the only known quarks were the up, the down, and the strange. After the charm [38, 39] and bottom [40] quarks were discovered in 1974 and 1977, respectively, the Kobayashi-Maskawa theory [11] of 1973 began to gain traction in the academic world. As discussed in Section 1.3.2, the theory predicted the CP violation in the Standard Model through the irreducible phase of the CKM matrix, so at least six quarks were needed, despite the knowledge of that time.

The 1980s marked the period in which the Cabibbo–Kobayashi–Maskawa (CKM) mechanism became increasingly established; in this context, the experimental observation of the unexpectedly long lifetime of B mesons [41] and the subsequent discovery of B^0–$\bar{B}^0$ mixing [42] provided enough motivation to employ B mesons as an ideal laboratory for testing the existence of the irreducible complex phase predicted by the CKM mechanism. Such studies required large samples of B mesons to reach the necessary statistical precision [29].

This necessity led to the creation of the *B-factories*: e^+e^- colliders specifically designed to operate at the center of mass energy at or below the mass of the the $\Upsilon(4S)$ resonance, a $(b\bar{b})$ bound state. In fact, the chosen value $\sqrt{s} \simeq m_{\Upsilon(4S)} \simeq 10.58\ \mathrm{GeV}/c^2$ is particularly advantageous, as it lies just above the threshold for the production of $B\bar{B}$ pairs with a branching fraction exceeding 96%. In Figure 3.1 the cross section of production of Υ states from e^+e^- collision.

The technological advances of the 1990s made it possible to realize the first two B-factories: KEKB at KEK (High Energy Accelerator Research Organization, Japan)

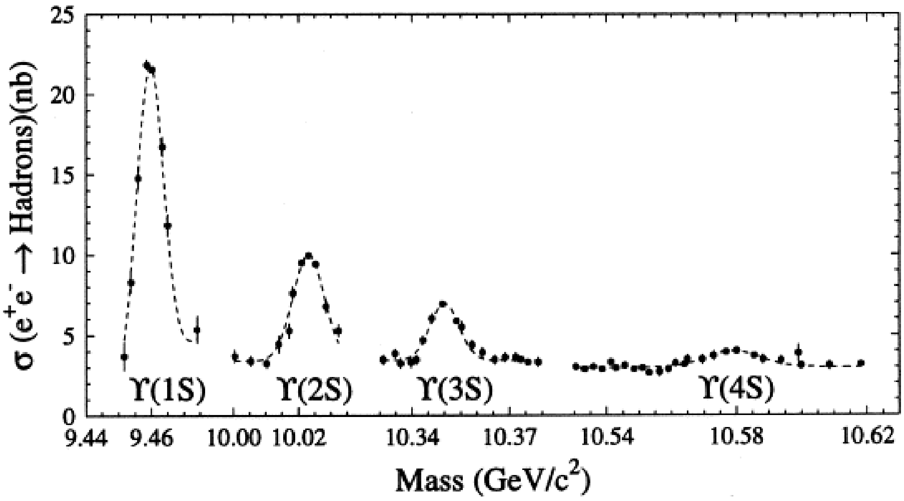

Figure 3.1: Production cross section of Υ states from $e^+e^- \to$ hadrons [43].

and PEP-II at SLAC (Stanford Linear Accelerator Center, USA). These facilities achieved instantaneous luminosities exceeding 10^{33} cm^{-2}s^{-1}, allowing the production of more than one million $B\bar{B}$ pairs per day.

At the $\Upsilon(4S)$ resonance, the production cross section for $e^+e^- \to \Upsilon(4S)$ is about 1.1 nb, while the cross section for $e^+e^- \to c\bar{c}$ at the same energy is slightly higher, around 1.3 nb. This makes B-factories also effectively charm-factories [44].

Currently, the SuperKEKB accelerator, the upgraded version of KEKB, is the only B-factory in operation.

3.2 The SuperKEKB Accelerator

Located at the KEK laboratory in Tsukuba, Japan, *SuperKEKB* is an upgraded asymmetric-energy e^+e^- double-ring collider 11 meters underground with a circumference of 3 kilometers. It comprises a 7-GeV electron ring, *High-Energy Ring* (HER), a 4-GeV positron ring, *Low-Energy Ring* (LER), and an injector *linear accelerator* (LINAC), and produces currently more than 40 $B^0\bar{B}^0$ and B^+B^- events every second, in approximately equal proportions, following in the footsteps of KEKB [45]. In Figure 3.2, a schematic representation of the SuperKEKB accelerator is shown.

Colliding beams of leptons imply a low QCD background and a precisely known collision energy, which sets stringent constraints on the collision's kinematic properties. Even though B^0 and $\bar{B}^0$ oscillate before decaying, their time-evolution is quantum-correlated in such a way that no B^0B^0 or $\bar{B}^0\bar{B}^0$ pairs are present at any time. Angular-momentum conservation implies that the decay of the spin-1 $\Upsilon(4S)$ in the two spin-0 bottom mesons yields total angular momentum $J = 1$. Because the simultaneous presence of two identical particles in an antisymmetric state would violate Bose statistics, the system evolves coherently as an oscillating $B^0\bar{B}^0$ particle-antiparticle pair until either one decays. This allows for the efficient identification of the bottom (or anti-bottom) content of one meson at the time of decay of the other. This important capability, known as *flavor tagging*, enables measurements of flavor-dependent decay rates, as required in many determinations of CP-violating quantities.

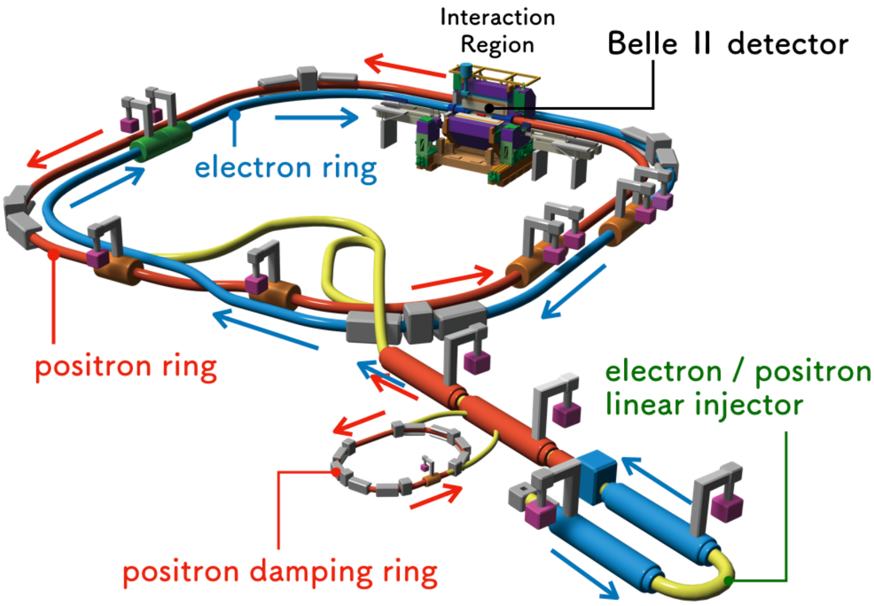

Figure 3.2: Illustration of SuperKEKB accelerator.

The SuperKEKB's asymmetric-energy design serves to measure the decay point of the B meson system. The Lorentz boost $\beta\gamma \simeq 0.28$ of the center of mass frame of the $\Upsilon(4S)$ results in a distance between the decay vertex of around 130 μm between the B mesons, in the laboratory frame, sufficient to identify both.

The intensity of particle collisions produced by accelerators is defined by the *instantaneous luminosity* (L), which is generally defined by the number of collisions per unit of time, the *interaction rate*

$$\frac{\mathrm{dN}}{\mathrm{dt}}\,[\mathrm{evt/s}] = L\,[\mathrm{cm}^{-2}\mathrm{s}^{-1}] \times \sigma\,[\mathrm{cm}^2]\,, \tag{3.1}$$

where σ is the cross section of the process. The instantaneous Luminosity can also be written as

$$L = \frac{N_b n_+ n_-}{4\pi\sigma_x^*\sigma_y^*} f_b R_L\,, \tag{3.2}$$

where N_b is the number of bunches inside the accelerator, $n_\pm$ is the number per bunch of positrons/electrons, $\sigma_{x/y}^*$ is the transverse bunch size at the IP, f_b is the frequency of bunch crossing, and R_L is a reduction factor accounting for geometrical efficiencies associated with the finite crossing angle and bunch length.

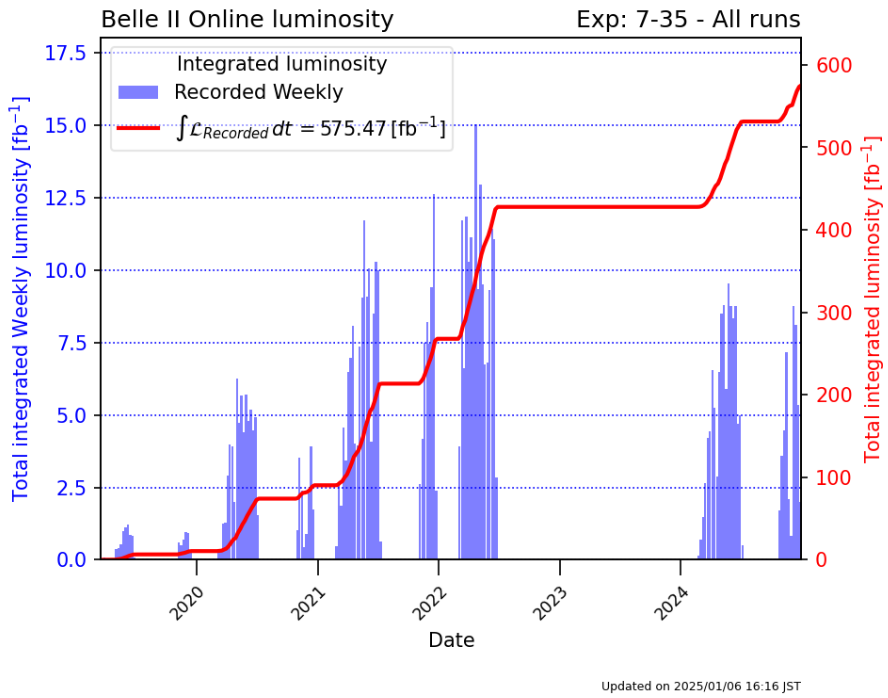

Figure 3.3: Total recorded integrated luminosity of Belle II [46].

The total number of events during a certain period T is obtained by integrating the previous equation, $N = L_{\text{int}} \times \sigma$. The integrated luminosity is defined as

$$L_{\text{int}} = \int_0^T L(t)\, \mathrm{d}t\,. \tag{3.3}$$

The instantaneous luminosity quantifies the rate at which particles interact per unit area and time, and in the December 2024 SuperKEKB accelerator achieved the record of $5.1 \times 10^{34}\ \text{cm}^{-2}\text{s}^{-1}$ [46], which is approximately 5/2 times higher than the luminosity of its predecessor, the KEKB accelerator. The instantaneous luminosity of SuperKEKB has grown over the past years, as shown in Figure 3.3. The goal is to reach $6 \times 10^{35}\ \text{cm}^{-2}\text{s}^{-1}$, that would allow Belle II to collect an integrated luminosity of 50 ab^{-1}. This goal is based on the implementation of the nano-beam scheme: in addition to increasing the beam currents, which contributes a factor of two to increasing the luminosity, the longitudinal beam overlap is also reduced. The decrease in the collision area is achieved by introducing a large crossing angle and maintaining an extremely small horizontal beam size.

3.3 Belle II Detector

The *Belle II detector* is located at the interaction point of the SuperKEKB collider. It is a multipurpose magnetic spectrometer. The detector has a cylindrical geometry, approximately 7 m long and 7 m in diameter, and is composed of several subdetectors arranged concentrically around the beam pipe, in Figure 3.4.

Closest to the interaction point lies the *vertex detector* (VXD), consisting of a two-layer pixel detector (PXD) and a four-layer silicon vertex detector (SVD),

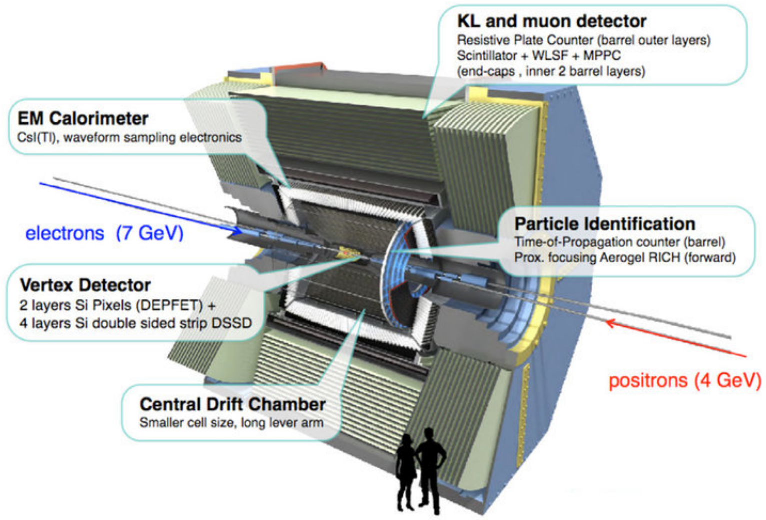

Figure 3.4: Schematic illustration of Belle II detector [47].

which provides excellent vertex resolution and tracking capabilities. Surrounding the VXD is the *central drift chamber* (CDC), a large-volume gas-based tracking system, designed to measure charged-particle trajectories and momenta with high precision and to contribute to particle identification via dE/dx measurements.

For hadron identification, Belle II employs two complementary Cherenkov detectors: the *time-of-propagation counter* (TOP) in the barrel region and the *aerogel ring-imaging Cherenkov detector* (ARICH) in the forward side. The *electromagnetic calorimeter* (ECL), composed of CsI(Tl) crystals, allows precise measurements of electromagnetic showers, crucial for detecting photons and electrons. All these subsystems are enclosed within a superconducting solenoid that generates a 1.5 T magnetic field. The outermost subsystem, the K_L^0 *and muon detector* (KLM), a multiple layers of resistive plate counters, identifies muons and long-lived neutral kaons.

3.4 Particle Reconstruction and Identification

The reconstruction and identification of particles in the Belle II experiment are performed using the information provided by the various subdetectors, in combination with dedicated algorithms implemented in the Belle II Analysis Software Framework (`basf2`) [48].

3.4.1 Particle Reconstruction

Charged particles such as electrons, muons, pions, kaons, and protons are reconstructed primarily through the tracking sub-detectors, VXD and CDC. Neutral particles are instead reconstructed via calorimetric information: photons and neutral pions are identified through electromagnetic clusters in the electromagnetic calorimeter (ECL), while muons, K_L^0 mesons, and neutrons are reconstructed using a combination of the ECL and the K_L^0 and muon detector (KLM).

Figure 3.5: Efficiency profile of the tracking system with respect to the transverse momentum of particles.

Track Reconstruction

The reconstruction of charged particles requires the accurate determination of their trajectory. Since VXD and CDC operate with different technologies, dedicated algorithms are employed for each system.

The reconstruction process begins with track finding, i.e. the identification of hit patterns that are compatible with the trajectory of a charged particle. Subsequently, a track fitting procedure is applied to extract the best estimates of the track parameters. At Belle II, the fitting is typically performed using a helix model, including multiple scattering and energy loss in the material, which is well suited to describe trajectories in the nearly homogeneous 1.5 T magnetic field. The precise knowledge of charge particles enables the reconstruction of the decay vertices of their parent particle.

Despite the use of advanced reconstruction algorithms, several challenges remain. Inefficiencies in the sub-detectors, as well as additional hits from beam-related backgrounds, can complicate the pattern recognition process. Moreover, the reconstruction of low-momentum tracks is particularly challenging: particles with transverse momenta below 200 MeV/c are strongly affected by multiple Coulomb scattering. Soft tracks with $p_T \lesssim 250$ MeV/c may also loop multiple times inside the CDC volume, producing additional spurious hits and complicating the track-finding procedure [49]. In Figure 3.5, the efficiency profile of the tracking system is shown with respect to the transverse momentum of particles.

Neutral Particles Reconstruction

Neutral particles are reconstructed from energy clusters in the ECL that are not associated with any charged-particle tracks. Since the geometrical acceptance of the ECL is larger than that of the tracking sub-detectors, neutral-particle candidates are typically required to be within the acceptance of the CDC, which has the narrowest acceptance among the sub-detectors. Because an ECL cluster provides only a single spatial point, its trajectory cannot be fully determined; therefore, the reconstruction algorithm assumes that the particle originates from the interaction point.

While photons typically produce symmetric electromagnetic showers in the ECL, hadrons can give rise to more complex and asymmetric shower shapes, often resulting in multiple clusters.

The reconstruction of neutral pions proceeds through the decay channel $\pi^0 \to \gamma\gamma$, obtained by combining two photon candidates. For π^0 mesons with energies below approximately 1 GeV, the angular separation of the decay photons is sufficiently large to yield two distinct, non-overlapping ECL clusters. At higher energies, up to about 2.5 GeV, the photons are more collimated and their showers may partially overlap; nevertheless, dedicated algorithms allow them to be reconstructed as separate photon candidates [50].

3.4.2 Particle Identification

Particle identification (PID) at Belle II relies on the complementary information provided by multiple subdetectors, each optimized for a different momentum range and particle type. The goal of PID is to distinguish efficiently between charged hadrons (pions, kaons, protons), leptons (electrons and muons), and photons, thereby enabling precise reconstruction of exclusive final states.

The main PID systems are the TOP, located in the barrel region, and the ARICH, installed in the forward end-cap. Both exploit Cherenkov radiation: the TOP determines the particle species from the propagation time of Cherenkov photons within quartz bars, while the ARICH utilizes aerogel as a radiator to reconstruct the Cherenkov rings of charged particles. Together, and using the specific ionization energy loss (dE/dx) measured in the CDC, these detectors provide excellent separation between **kaons** and **pions**.

Lepton identification relies on a combination of tracking and calorimetric information. **Electrons** are identified by the shower shape, the energy deposition in the ECL, and the matching between the track momentum and the calorimeter cluster energy. **Muons** are recognized by their penetration depth into the outer KLM detector.

Photons are identified as isolated energy clusters without associated tracks, while neutral pions are reconstructed from the invariant mass of two photon candidates. In addition, the KLM contributes to the reconstruction of $\boldsymbol{K_L^0}$ mesons, which are identified through their characteristic late interactions in the outer detector layers.

3.5 CP Asymmetry in the $D^0 \to \pi^+\pi^-\pi^0$ Decay

To measure CPV, we need to determine the flavour of the neutral D meson at production. Since the final state is the same for D^0 and $\bar{D}^0$, we reconstruct the D^0 from the decays $D^{*+} \to D^0\pi^+_{\text{tag}}$ and $D^{*-} \to \bar{D}^0\pi^-_{\text{tag}}$, originating from a $c\bar{c}$ event, in Figure 3.6. The charge of the tagging pion ($\pi^\pm_{\text{tag}}$) allows us to determine the initial flavour of the neutral D meson. Due to its low momentum, the π_{tag}, commonly referred to as the *soft pion*, is more difficult to detect experimentally than the other pions in the final state.

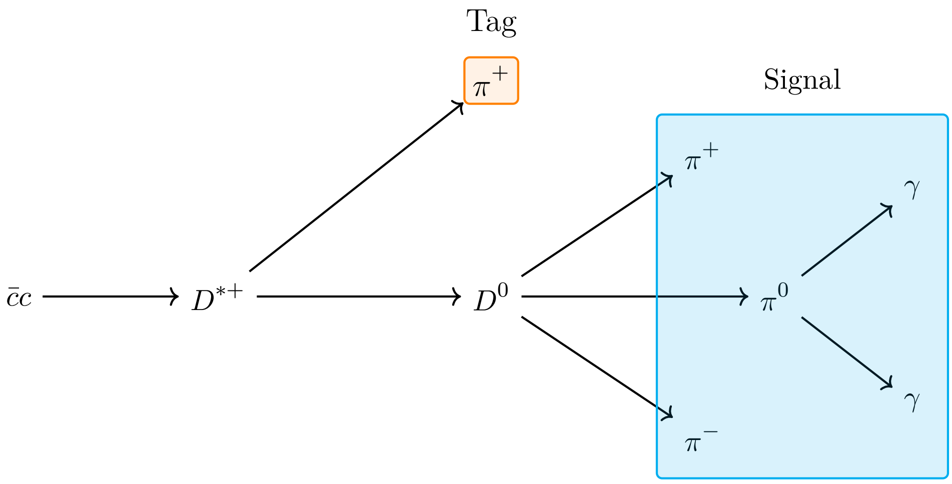

Figure 3.6: Visual decay chain of $c\bar{c}$ to D^0

One advantage of using D^* decay is the availability of a variable with a strong background reject power, $\Delta M = m(D^*) - m(D^0)$.

The asymmetry that is directly measured is the *raw asymmetry*:

$$\mathcal{A}_{\text{raw}} = \frac{N(D^0 \to \pi^+\pi^-\pi^0) - N(\bar{D}^0 \to \pi^+\pi^-\pi^0)}{N(D^0 \to \pi^+\pi^-\pi^0) + N(\bar{D}^0 \to \pi^+\pi^-\pi^0)}, \tag{3.4}$$

where $N(i \to f)$ indicates the number of decays observed from an initial state i to a final state f. Usually, N is extracted with a fit to the invariant mass (of the ΔM) distributions of the D^0 and the $\bar{D}^0$.

The experimental observable $\mathcal{A}_{\text{raw}}$ differs from the pure CP asymmetry $\mathcal{A}_{CP}$ because of additional nuisance asymmetries induced by the reconstruction ($\mathcal{A}_{\text{det}}$) and the detector setup ($\mathcal{A}_{\text{prod}}$):

$$\mathcal{A}_{\text{raw}} \simeq \mathcal{A}_{\text{prod}} + \mathcal{A}_{\text{det}} + \mathcal{A}_{\text{CP}}\,. \tag{3.5}$$

We now proceed to discuss these two terms.

3.5.1 The Production Asymmetry

The production asymmetry arises from a purely physical effect: the interference between the Z^0 and γ gauge bosons in the process $e^+e^- \to c\bar{c}$, as illustrated in

Figure 3.7.

The non-uniform angular distribution, due to the weak current contribution in $c\bar{c}$ events, leads to a difference in the hadronization of charm quarks and consequently to an asymmetry in the production of D^{*+} and D^{*-} mesons, so D^0 and $\bar{D}^0$.

In particular, in the collision center-of-mass (CM) frame, the $\bar{c}$ quark is more likely to be produced in the direction of the incoming electrons—*i.e. forward*—while the c quark tends to be produced in the direction of the outgoing positrons—*i.e. backward*. For this reason, the production asymmetry is also referred to as the *Forward-Backward Asymmetry*.

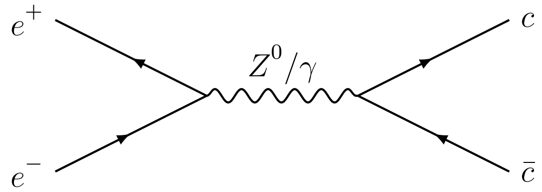

Figure 3.7: Visual interference in the $e^+e^- \to c\bar{c}$ process.

This production asymmetry manifests itself in experimental measurements when the detector does not provide complete geometrical detection, i.e. when the acceptance is smaller than 4π, as is the case for the Belle II detector.

Starting from the differential cross section of the $e^+e^- \to c\bar{c}$ process, it is possible to derive the so-called Forward-Backward Asymmetry, denoted by $\mathcal{A}_{\text{FB}}$

$$\frac{\mathrm{d}\sigma}{\mathrm{d}\cos\theta_{\text{CM}}} \propto 1 + \cos^2\theta_{\text{CM}} + \frac{8}{3}\mathcal{A}_{\text{FB}}\cos\theta_{\text{CM}}\,. \tag{3.6}$$

$\mathcal{A}_{\text{prod}}$ is as an odd function of $\cos\left(\theta_{\text{CM}}\right)$, where θ_{CM} is the polar angle of the reconstructed D^* meson with respect to the beam axis in the CM frame:

$$\mathcal{A}_{\text{prod}} = \frac{8}{3}\mathcal{A}_{\text{FB}}\frac{\cos\theta_{\text{CM}}}{1 + \cos^2\theta_{\text{CM}}}\,. \tag{3.7}$$

In absence of detection asymmetry: $\mathcal{A}'_{\text{raw}} = \mathcal{A}_{\text{prod}} + \mathcal{A}_{\text{CP}}$. A common method to remove to remove $\mathcal{A}_{\text{det}}$ is to measure at leat two bins in $\cos\theta_{\text{CM}}$, $\mathcal{A}'_{\text{raw}}(\cos\theta_{\text{CM}} > 0)$ and $\mathcal{A}'_{\text{raw}}(\cos\theta_{\text{CM}} < 0)$, and then average the two. With this method, the production asymmetry cancels and only $\mathcal{A}_{\text{CP}}$ survives.

3.5.2 The Detection Asymmetry

A different detection efficiency between D^0 and $\bar{D}^0$ mesons may arise from both hardware conditions and software algorithms. On the hardware side, factors such as the detector's operational status and geometrical configuration can introduce biases in measurements. On the software side, reconstruction algorithms and the selection criteria applied to signal candidates can produce asymmetries in the identification or reconstruction of the two D neutral mesons.

These factors collectively contribute to differences in the overall reconstruction efficiency, leading to detection asymmetries. It is therefore worthwhile to briefly outline the primary sources that can affect the reconstruction efficiency.

The final state particles measured in the detector are the charged pions from the D^* and the neutral D decays, and the photons from the π^0 decay.

Two principal components govern the reconstruction efficiency of charged particles: the probability of correctly reconstructing the particle's trajectory, referred to as *tracking efficiency*, and the capability to correctly identify the particle type through particle identification (PID) algorithms, referred to as *PID efficiency*.

The tracking efficiency depends on the performance of the tracking sub-detectors and is influenced by the number and position of detector layers the particle traverses. Similarly, the PID efficiency is shaped by the detector's ability to distinguish among different particle species based on their interaction signatures.

Both tracking and PID efficiencies exhibit a dependence on the particle's electric charge. Charged particles with opposite signs can follow different paths in a magnetic field and interact differently with the detector material. As a result, a *charge asymmetry* may arise, which can lead to biased measurements of physical observables.

It is therefore essential to accurately understand and measure these efficiencies to ensure unbiased measurements and a correct interpretation of experimental results.

For the signal channel, $D^* \to D^0\pi^+_{tag}$, $D^0 \to \pi^+\pi^-\pi^0$, the only significant source of detection asymmetry is the reconstruction of the tag pion. To measure it and count it, control channels like the CF $D^0 \to K\pi$, with and without the D^* tagging, are used. This topic is not discussed further, as it falls beyond the scope of this work.

Chapter 4

The Analysis

The chapter describes the main part of my work: an estimation of the statistical uncertainty and possible significance of the CP asymmetry measured in different regions of the DP. It begins with a description of the dataset and selection criteria I used in the work. It continues highlighting the effects of detector response with a study of the reconstruction efficiency on the observed distributions.

Subsequently, the focus is placed on the low-energy region of the Dalitz plot, where the contribution of the $\rho^{\pm}(770)$ resonances dominates. Three different regions of the Dalitz plot are defined and characterised in terms of reconstruction efficiency, statistical yield, and statistical uncertainty on the CP asymmetry.

I have used the predictions of the theoretical paper presented in Section 2.4 to compute the average expected CP asymmetry. Finally, the significance of the predicted CP asymmetry is evaluated, providing estimates of the luminosity required to achieve target sensitivity levels.

4.1 Dataset

The analysis presented in this work is performed using the official Monte Carlo (MC) generated dataset provided by the Belle II collaboration.

The software infrastructure adopted for the simulation and data processing is the Belle II Analysis Software Framework (*basf2*) [48], which provides detector simulation, event reconstruction, and physics analysis. This framework integrates several external libraries and tools essential for high-energy physics simulations. Among them, event generation is handled by: EvtGen [51] for decay modelling and PHOTOS [52], KKMC [53], PYTHIA8 [54] for additional physics effects. Geant4 [55] is used for modeling the interactions between particles and detector material. The ROOT [56] framework itself is used extensively for data storage, histogramming, and analysis operations.

The MC sample consists of no-CP violating signal events from the process $e^+e^- \to c\bar{c}$, in which at least one D^{*+} meson (or its CP-conjugate state) is produced and subsequently decays to $D^0\pi^+$, with the D^0 further decaying into $\pi^+\pi^-\pi^0$, while the other charm quark hadronizes and decay generically. The dataset contains 13×10^6 signal events of D^0 and $\bar{D}^0$. Since $\sigma(e^+e^- \to D^{*+}X) \simeq 290$ pb^{-1} [57] at $\sqrt{s} \simeq 10.5$ GeV/c, and the branching ratio $BR(D^{*+} \to D^0\pi^+, D^0 \to \pi^+\pi^-\pi^0) \simeq 1\%$ [8], the dataset corresponds to an integrated luminosity of 2.2 ab^{-1}, which is slightly more than five times the integrated luminosity collected by Belle II in its first Run (Run1, 2019-2022, 424 fb^{-1}). It is essential to note that only the signal is utilized, and no background samples have been included in the present study.

I have used two types of ntuples created from the same dataset:

- generated candidate: this ntuple contains information on the generated values of momentum, charge, and many other properties of all the particles of the signal channel;

- reconstructed candidate: this ntuple contains information on the reconstructed values of momentum, charge, and many other properties of all the particles of the signal channel. The generated particles are first passed to the simulation part of basf2, which simulates the interaction of particles with the detector. Then, the simulated detector signals are passed to the basf2 reconstruction algorithms, which produce a list of particles (and their properties), just as they do with real data.

In this work, I processed the above-mentioned ntuples using the ROOT framework, with custom code developed in C++ and Python to handle and analyze the various ROOT files involved.

4.1.1 Selection Criteria

To enable a more efficient analysis and optimize the use of computational resources, a preliminary selection of loose cuts is usually applied to real data. This procedure produces the *skimmed* dataset, which discards most of the backgrounds, while retaining basically all the signal. Even if this operation is not needed for our signal sample, we still apply it to avoid introducing any differences between the simulation and a possible future analysis on the data. The skimming is summarised in Appendix A.

I applied the selection criteria used for a very recent result on the DP-integrated $\mathcal{A}_{\mathrm{CP}}$ in $D^0 \to \pi^+\pi^-\pi^0$ decay presented at the EPS conference this year [58]. Only candidates that are associated with the MC generated signal D^{*+} or D^{*-} are used, so only candidates that were correctly reconstructed. In the following, I briefly describe the selection. Only *prompt* $D^{*\pm}$ mesons (i.e., those produced directly in $e^+e^- \to c\bar{c}$ processes), assuming that they originate from the Interaction Region (IR), are retained for the analysis. $D^{*\pm}$ mesons originating from $B \to D^*Y$ decays can be vetoed by exploiting their limited momentum in the centre-of-mass (CM) frame. This is achieved using the variable

$$X = \frac{p_{\mathrm{CM}}}{p_{\mathrm{CM}}^{\max}(\sqrt{s})}\,, \tag{4.1}$$

where p_{CM} is the momentum of the D^* in the CM frame and $p_{\mathrm{CM}}^{\max}(\sqrt{s})$ is its kinematic maximum at the given centre-of-mass energy. For events at the $\Upsilon(4S)$ resonance, the maximum momentum of a D^* is approximately $p_{\mathrm{CM}}^{\max} \simeq 2.6$ GeV/c; therefore, a requirement of $X > 1.06$ is imposed. After this cut, signal events containing at least one D^*, from B, candidate constitute roughly 1% of all reconstructed D^* decays. Tracks of charged mesons are required to originate near the IP. Specifically, the transverse distance of closest approach of the track helix to the IP, d_r, must be less than 0.5 cm, and the longitudinal impact parameter $|d_z|$ must be less than 1 cm. All tracks are required to be reconstructed within the acceptance of the Central Drift Chamber (CDC), which corresponds to a polar angle θ in the range $17^\circ < \theta < 150^\circ$. Tracks are also required to be compatible with the pion mass hypothesis to reduce the background arising from the misidentification of kaons as pions. Photons and neutral pions are identified solely via their energy deposition in the electromagnetic calorimeter (ECL). To improve the signal purity, a selection is applied to each cluster based on the number of associated hits, the time of arrival, and the time significance, defined as the ratio between the cluster time and its uncertainty. ECL cluster shapes are also used to reject background, since photon-induced clusters are typically narrower than those produced by other particles. Then, a Zernike multivariate analysis is employed to further discriminate between photon clusters and those originating from K_L mesons.

Further requirements are applied to reconstructed masses and momenta:

- $\Delta M = M_{D^*} - M_{D^0}$ is required to lie between 140 and 150 MeV/c^2,
- M_{D^0} between 1.785 and 1.95 GeV/c^2,
- M_{π^0} between 116 and 150 MeV/c^2,
- $|\vec{p}_{\pi^0}|$ above 500 MeV/c,
- E_γ above 100 MeV.

After having applied all the selection criteria, the reconstructed ntuple of D^0 and $\bar{D}^0$ is composed of $n_{reco} = (1.621 \pm 0.001) \times 10^6$ candidates. In Figure 4.1 the ΔM of only the D^0 ntuple is shown.

4.2 Dalitz Plots

With the selected signal sample, I produced the Dalitz plots for both the generated D^0 and the $\bar{D}^0$, shown in Figure 4.2. As expected, they are compatible with the plots produced with *Laura*$++$, confirming that the model implemented in the Belle II generator correctly reproduces the expected structure. This was an important check, since the Dalitz structure of the signal channel was only recently implemented in the generator.

To compare the D^0 and the $\bar{D}^0$ Dalitz plots, we need to consider that D^0 decays are connected to $\bar{D}^0$ decays by the CP-conjugation operation:

$$CP\left|D^0 \to \pi^+\pi^-\pi^0\right\rangle = \left|\bar{D}^0 \to \pi^-\pi^+\pi^0\right\rangle .$$

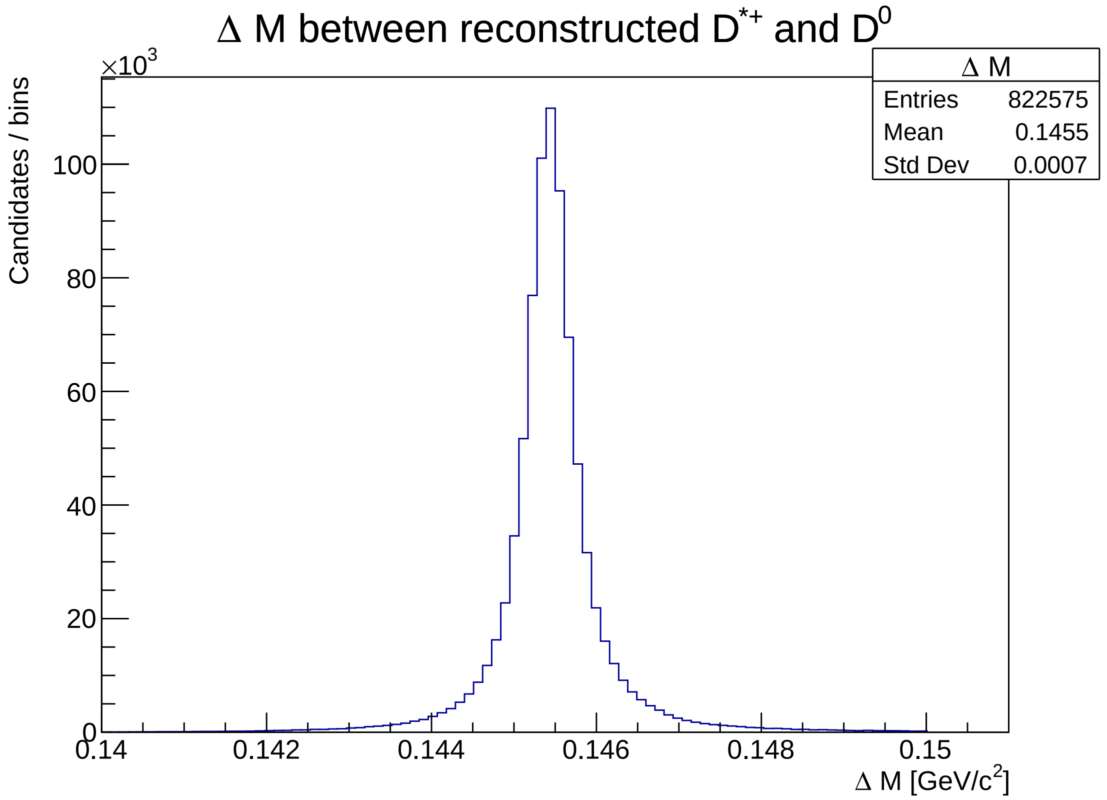

Figure 4.1: ΔM of reconstructed signal candidates of D^{*+} and D^0.

CP-conjugation corresponds to the exchange of the π^+ daughter of D^0, with the π^- daughter of $\bar{D}^0$. In other words:

$$m(\pi^+\pi^0)[D^0] \equiv m(\pi^-\pi^0)[\bar{D}^0] \quad \text{and,}$$
$$m(\pi^+\pi^0)[\bar{D}^0] \equiv m(\pi^-\pi^0)[D^0]\,.$$

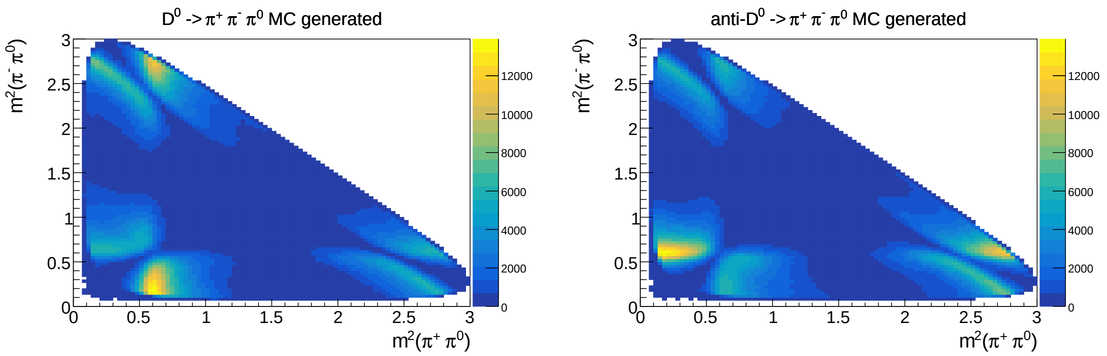

Figure 4.2: Plots of 6.4×10^6 generated decays of D^0 (left) and 6.4×10^6 generated decays of $\bar{D}^0$ (right) from the dataset. 90×90 bins.

Figure 4.3 shows the Dalitz plot I obtained with the reconstructed sample. The differences with the generated distribution arising from the reconstruction efficiency will be discussed in Section 4.3. The focus of this study, as mentioned in Section 2.4, is the region at low invariant masses below 1 GeV^2, in Figure 4.4. In this region, only $\rho^{\pm}(770)$ resonances contribute.

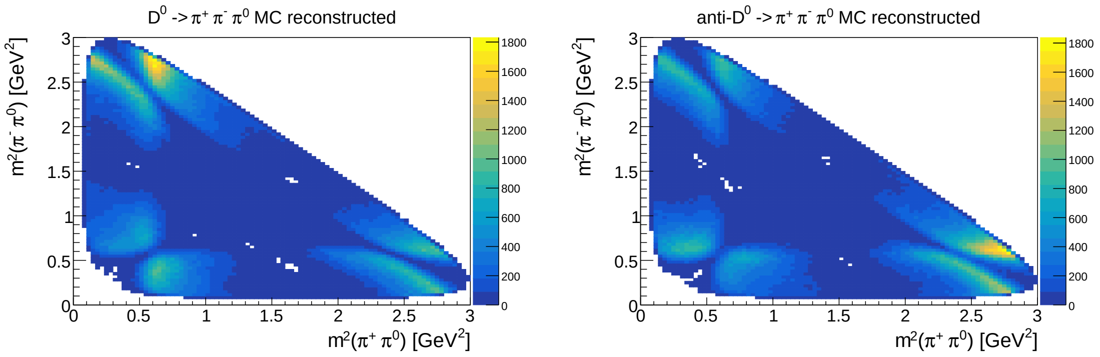

Figure 4.3: Plots of $\simeq 800 \times 10^3$ reconstructed decays of D^0 and $\simeq 800 \times 10^3$ decays of $\bar{D}^0$ from the dataset. 90×90 bins.

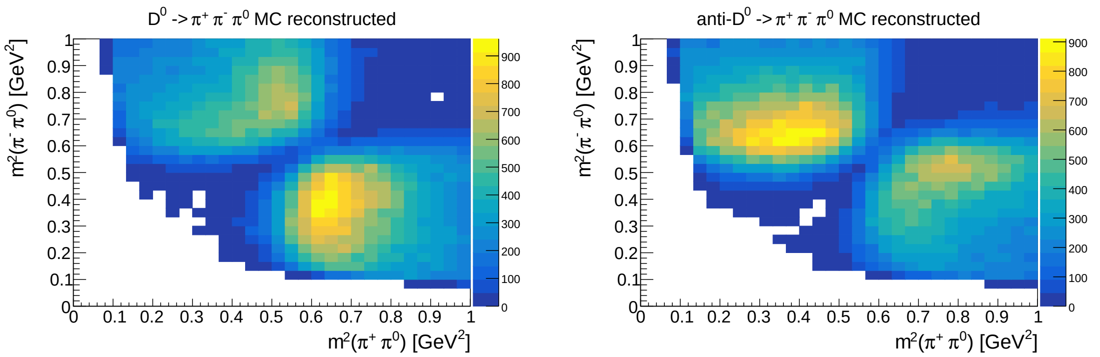

Figure 4.4: Plots of $\simeq 180 \times 10^3$ reconstructed decays of D^0 and $\simeq 180 \times 10^3$ decays of $\bar{D}^0$ in a limited region. 30×30 bins.

4.3 Efficiency Study

It is convenient to introduce a parameter that quantifies the probability of correctly reconstructing a signal decay. This parameter is the *reconstruction efficiency*, defined as the ratio between the number of successfully reconstructed candidates and the total number of generated candidates:

$$\varepsilon \equiv \frac{N_{\text{reco}}}{N_{\text{gen}}}, \qquad \sigma_{\varepsilon} = \sqrt{\frac{\varepsilon(1-\varepsilon)}{N_{\text{gen}}}}. \tag{4.2}$$

The standard deviation is obtained by considering that the number of reconstructed candidates follows a binomial distribution with probability ε.

In the full DP the total number of generated D^0 and $\bar{D}^0$ is $n_{\text{tot}(gen)} = 12.780 \times$

10^6, corresponding to a luminosity of 2.2 ab^{-1}. The reconstructed candidates are $n_{\text{tot}(reco)} = (1.621 \pm 0.001) \times 10^6$, with an efficiency of $\varepsilon = (12.66 \pm 0.01)\%$. For the luminosity of 50 ab^{-1}, the goal integrated luminosity of Belle II, since N scales linearly with the luminosity, the extrapolated values are $n_{\text{tot}(gen)} = 191.72 \times 10^6$, and $n_{\text{tot}(reco)} = (36.95 \pm 0.01) \times 10^6$.

An attempt was made to study the dependence of efficiency on kinematic variables. I have noted, in Figure 4.5, that the kinematic variables were not independent. This means the study of the efficiency of D^0 and its daughters can not be considered independent. Instead, the efficiency that I plotted for a single particle depends on the efficiency of reconstructing the entire decay chain, from the D^* to the end.

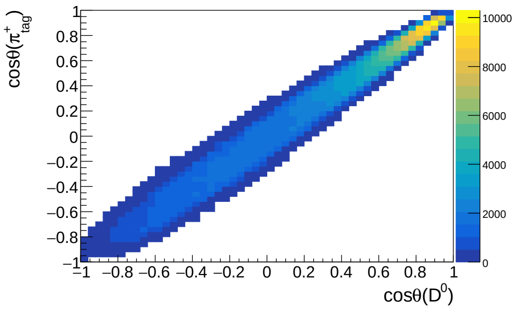

(a) Number of reconstructed D^0 decays in terms of $\cos\theta(D^0)$ and $\cos\theta(\pi^+_{\text{tag}})$.

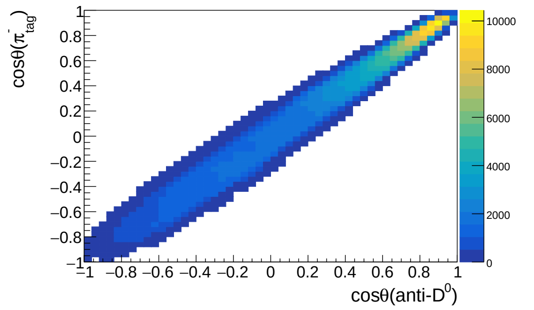

(b) Number of reconstructed $\bar{D}^0$ decays in terms of $\cos\theta(\bar{D}^0)$ and $\cos\theta(\pi^-_{\text{tag}})$.

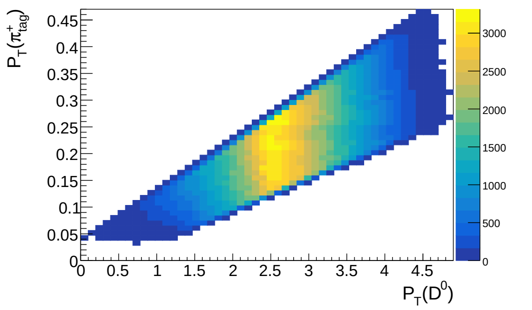

(c) Number of reconstructed D^0 decays in terms of transverse momenta $\mathrm{P}_T(D^0)$ and $\mathrm{P}_T(\pi^+_{\text{tag}})$.

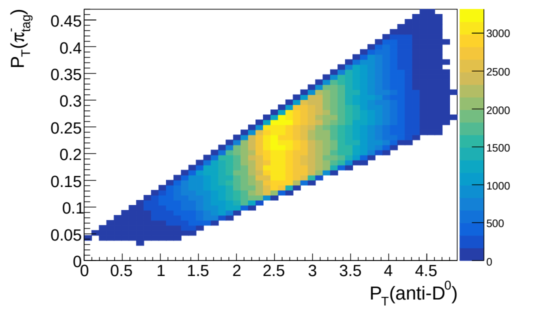

(d) Number of reconstructed $\bar{D}^0$ decays in terms of transverse momenta $\mathrm{P}_T(\bar{D}^0)$ and $\mathrm{P}_T(\pi^-_{\text{tag}})$.

Figure 4.5: Number of reconstructed candidates in terms of $\cos\theta$ and the transverse momentum of the D^0 and π_{tag}. 90×90 bins.

In Figure 4.6, the reconstruction efficiency of the D^{*+} and D^{*-} signal decays on the Dalitz plot is presented. The overall efficiency stays below 18%, and depends on the kinematic region of the Dalitz plot. In particular, a significant reduction in efficiency is observed in the low-energy domain, i.e. for squared invariant masses below 1 GeV^2, shown in Figure 4.7. This behaviour is attributed to the presence of low-momentum neutral pions, whose decay photons are difficult to reconstruct due to limited detector resolution and increased background contamination, thereby reducing the probability of successfully reconstructing the full decay chain.

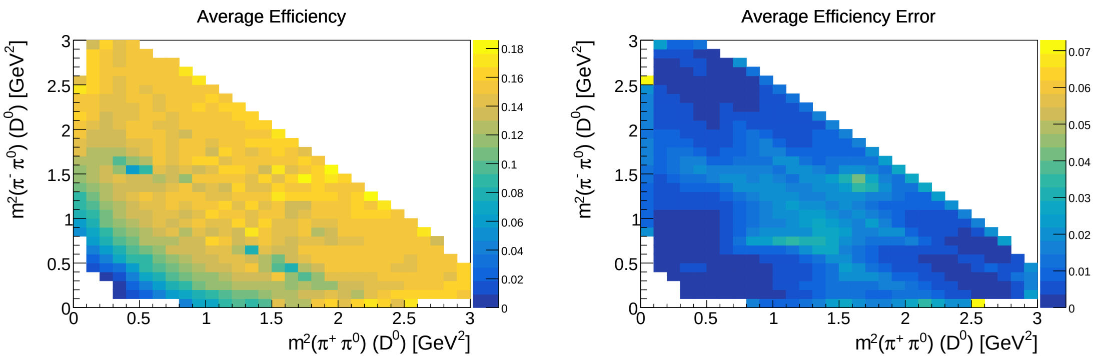

Figure 4.6: Two-dimensional distributions of the reconstruction efficiency for D^0 and $\bar{D}^0$ decays, together with the corresponding statistical uncertainties. The axes are referred to D^0 pions. 30×30 bins.

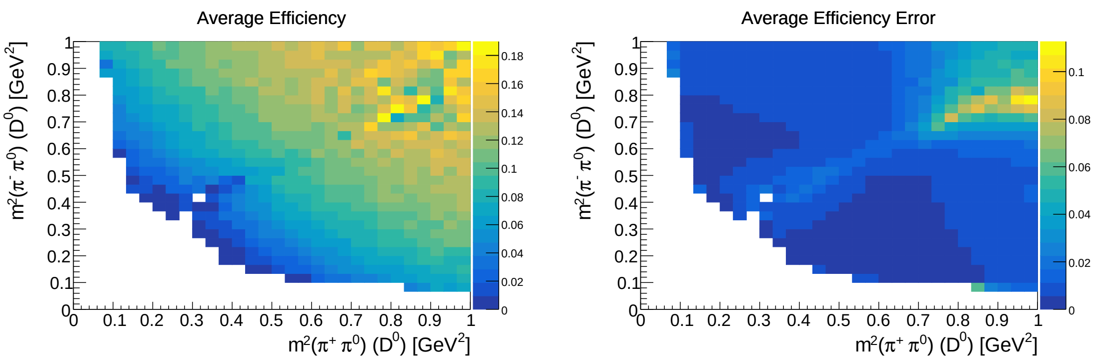

Figure 4.7: Two-dimensional distributions of the reconstruction efficiency for D^0 and $\bar{D}^0$ decays in a limited region of the Dalitz, together with the corresponding statistical uncertainties. The axes are referred to D^0 pions. 30×30 bins.

In Figures 4.8 the efficiency asymmetry between the (D^0, π^+) and $(\bar{D}^0, \pi^-)$ pairs as a function of the transverse momentum p_T is reported.

4.4 Different Regions of the Dalitz Plot

Following the theoretical model, the study was thus restricted to specific regions of the Dalitz plot below 1 GeV^2 in both the Dalitz variables.

In total, three different regions of interest are defined and illustrated in Figure 4.9. The Square is a CP-symmetric region between D^0 and $\bar{D}^0$, defined by cuts that are symmetric with respect to the bisector of the plane formed by the squared invariant masses.

A different approach was required for the triangular regions, which are not symmetric under CP conjugation, and thus the two regions are not automatically comparable. To properly identify the corresponding kinematic regions for D^0 and $\bar{D}^0$, the charged pions were swapped, associating the π^+ of the D^0 decay with the π^- of the $\bar{D}^0$ decay. These selections are reported in Table 4.1.

For these regions, I reported in Table 4.2 the number of reconstructed candi-

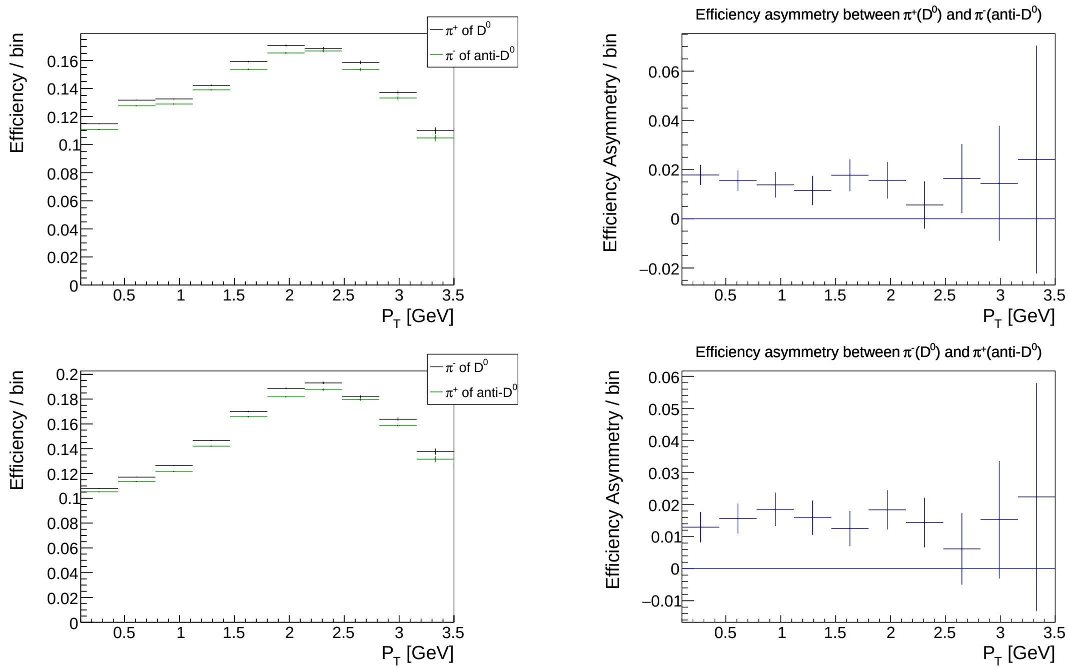

Figure 4.8: Reconstruction efficiencies and their asymmetry of the charged pions daughters of $\pi^{\pm}$ of D^0 and $\bar{D}^0$ as a function of the transverse momentum p_T. The asymmetry is defined bin-by-bin as the relative difference between the two channels.

Portion	**Criteria**
Square	$m^2_{\pi^+\pi^0}, m^2_{\pi^-\pi^0} < 1\ \mathrm{GeV}^2$
Triangle 1	$m^2_{\pi^+\pi^0}, m^2_{\pi^-\pi^0} < 1\ \mathrm{GeV}^2$ $m^2_{\pi^-\pi^0} < m^2_{\pi^+\pi^0}$
Triangle 2	$m^2_{\pi^+\pi^0}, m^2_{\pi^-\pi^0} < 1\ \mathrm{GeV}^2$ $m^2_{\pi^-\pi^0} > m^2_{\pi^+\pi^0}$

Table 4.1: Definition of different Dalitz regions in the low-energy Dalitz. For the Triangle 1 and 2, the criteria are referred to D^0 pions. To obtain the criteria for the $\bar{D}^0$, it needs to swap the charged pions.

dates and the reconstruction efficiency that is $\sim 3\%$ lower than the total efficiency, considering the whole DP.

4.5 The Expected Average Asymmetry

For each of the regions in Section 4.4, the expected average asymmetry was computed, consistently with the theoretical prediction.

I considered ten distinct constant-asymmetry regions c_i, illustrated in Figure 4.10

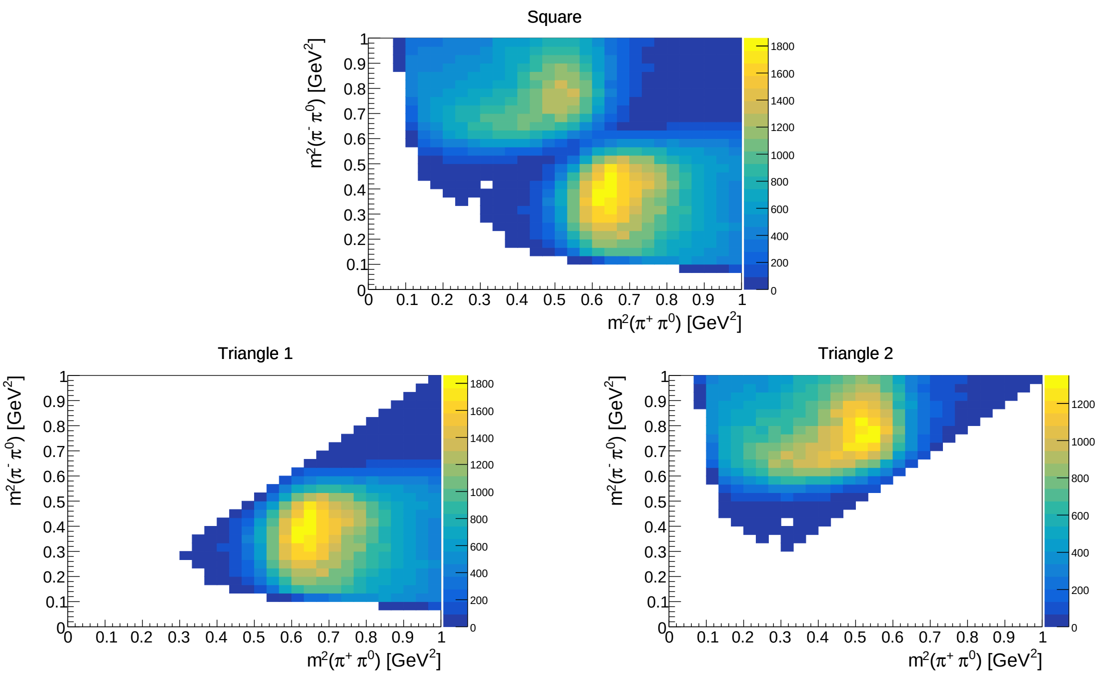

Figure 4.9: The different Dalitz regions in low-energy region of D^0 and $\bar{D}^0$ reconstructed decay candidates. The axes are referred to D^0 pions. The Square, Triangle 1 and 2 are 30×30 bins.

Portion	$\boldsymbol{n_{\text{tot}}}$ **[$\times 10^3$]**	**Efficiency ε [%]**
Square	356.2 ± 0.6	8.28 ± 0.01
Triangle 1	199.4 ± 0.4	9.25 ± 0.01
Triangle 2	157.0 ± 0.4	7.31 ± 0.02

Table 4.2: Table of the Efficiency of the sample for different regions of the low-energy Dalitz plot. $n_{\text{tot}} = n_{D^0} + n_{\bar{D}^0}$ is the total number of reconstructed candidates of signal.

(each corresponding to a different interval highlighted in the colour map), and I assigned to each one the mean value of the predicted CP asymmetry, reported in Table 4.3. As an example, for the darkest blue region c_{10}, defined between $\mathcal{A}_{\mathcal{CP}} = -5 \times 10^{-4}$ and $\mathcal{A}_{\mathcal{CP}} = -2.5 \times 10^{-4}$, the average value $\mathcal{A}_{\mathcal{CP}}(c_{10}) = -3.75 \times 10^{-4} = -0.0375$ % was used.

The *Expected Average Asymmetry* is defined as

$$\mathcal{A}_{\text{avg}} = \sum_i \mathcal{A}_{CP}(c_i) \frac{(n_i + \bar{n}_i)}{n_{\text{tot}}}\,, \tag{4.3}$$

where $A_{(c_i)}$ is the expected CP asymmetry in region c_i, n_i ($\bar{n}_i$) is the number of reconstructed D^0 ($\bar{D}^0$) candidates in region c_i, and n_{tot} is the total number of D^0 and $\bar{D}^0$ candidates in the selected region (Square, Triangle 1, Triangle 2).

The next challenge to face is thus to evaluate, for each region, the reconstructed yields at the Belle II, namely the quantities n_i and $\bar{n}_i$.

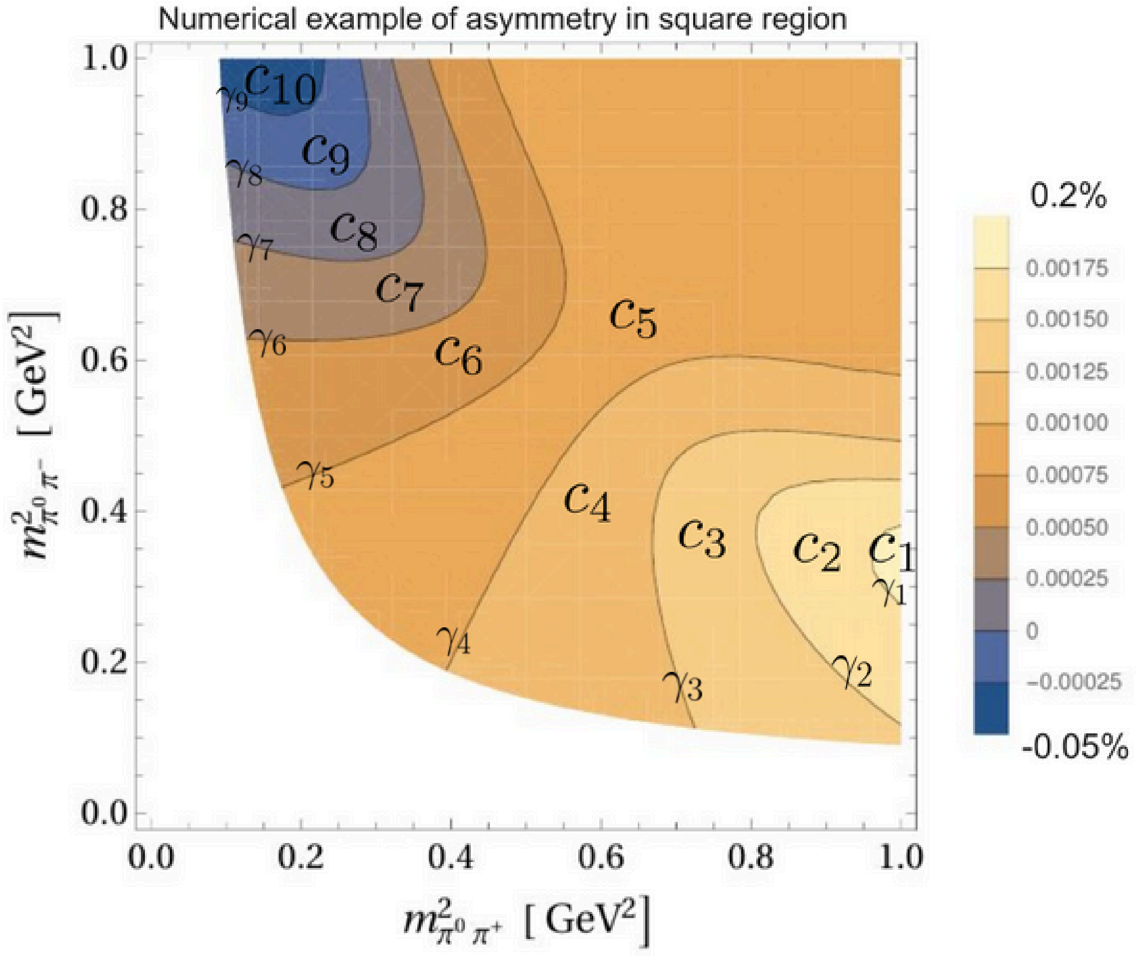

Figure 4.10: Definition of the CP asymmetry constant regions of the theoretical prediction of Section 2.4.

Region	c_1	c_2	c_3	c_4	c_5
$\mathcal{A}_{\mathcal{CP}}(c_i)$ [%]	0.1875	0.1625	0.1375	0.1125	0.0875
Region	c_6	c_7	c_8	c_9	c_{10}
$\mathcal{A}_{\mathcal{CP}}(c_i)$ [%]	0.0625	0.0375	0.0125	-0.0125	-0.0375

Table 4.3: Numerical values of CP asymmetry in the constant CP asymmetry regions of the theoretical prediction.

4.5.1 Analytical Definition of the Constant-Asymmetry Regions

The initial step of the analysis defines the c_i regions of Figure 4.10 in an analytical form. The exact functional expressions of the region boundaries were not explicitly mentioned in the paper. Therefore, the contours of the regions were sampled using an image-processing tool to extract data points from the image and then fitted with polynomial functions to reproduce the shape of the boundaries. In some cases, however, the curves could not be directly described by a single function, as they do not satisfy the definition of a function in the given coordinate system. To address this, the sampled points were either divided into smaller subsets or the coordinate axes were rotated, sometimes both, to be successfully fitted by a function.

Below are listed the polynomial expressions used to describe the curves γ_i, the boundaries of the c_i regions. When the data sample is split into the subsets mentioned above, the curves are referred to as $\gamma_{i.a(b)}$ for the two parts:

- second order polynomial for: $\gamma_{9.a}$;
- third order polynomial for: γ_1, $\gamma_{6.a}$, $\gamma_{7.a}$;
- fourth order polynomial for: $\gamma_{9.b}$;
- fifth order polynomial for: γ_5, $\gamma_{6.b}$, $\gamma_{7.b}$, $\gamma_{8.a}$, $\gamma_{8.b}$;
- the function $f(x) = \dfrac{d}{x-g} + c \times x^2 + b \times x + a$ for: γ_2, $\gamma_{3.a}$, γ_4.

At this stage, only the boundaries of the regions are defined. For the case of the D^0 mesons, the region c_i with $i < 4$ is constructed as the area enclosed between the curves γ_i and γ_{i-1}. Analogously, for regions c_i with $6 \leq i \leq 10$, the definition is given by the area between the curves γ_{i-1} and γ_i. As a concrete example, the region c_1 corresponds simply to the area below the curve γ_1, whereas the region c_4 is obtained as the difference between the area below γ_4 and that below γ_3. The same construction applies to regions c_6 through c_{10}. The result of this procedure is illustrated in Figure 4.11, which shows the areas under two consecutive curves, and in Figure 4.12, which highlights the region defined by their difference .Every bin is filled only with candidates inside selected regions; for this reason, bins that are across the γ_i curves have less candidates.

For the $\bar{D}^0$ mesons, the regions are defined in the same manner but are related to those of the D^0 by swapping the two DP axes. Consequently, when displayed on the same plot, the $\bar{D}^0$ regions appear as the transposed counterparts of those defined for the D^0.

The definition of region c_5 required a slightly different procedure. In the case of the D^0, I obtained the region by taking the area above the curve γ_4 and subtracting the region above the curve γ_5.

I then reported the resulting number of reconstructed candidates, $n_i + \bar{n}_i$, obtained from the data sample corresponding to an integrated luminosity of $L_{\text{int}} = 2.2\ \text{ab}^{-1}$, for each c_i region of the Square in Table 4.4. The total number of reconstructed candidates, n_{tot}, is given separately in Table 4.2.

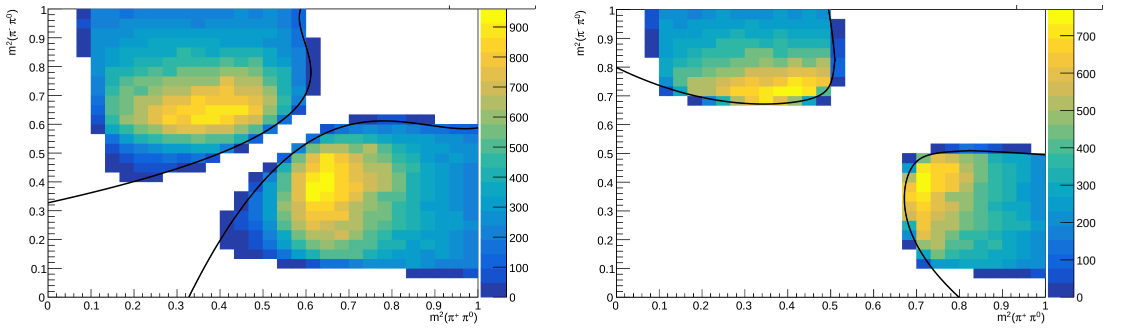

Figure 4.11: Plot of generated events of D^0 and $\bar{D}^0$ decays with values under the curves γ_4 (on the left) and γ_3 (on the right). 30×30 bins. Every bin is filled only with events inside selected regions; for this reason, bins that are across the γ_i curves have less candidates.

Region	c_1	c_2	c_3	c_4	c_5
$n_i + \bar{n}_i$ $[\times 10^3]$	1.20 ± 0.03	22 ± 5	69.2 ± 0.3	95.3 ± 0.3	54.4 ± 0.2
Region	c_6	c_7	c_8	c_9	c_{10}
$n_i + \bar{n}_i$ $[\times 10^3]$	50.2 ± 0.2	33.2 ± 0.2	17.6 ± 0.1	9.1 ± 0.1	2.82 ± 0.05

Table 4.4: Number of reconstructed events inside every region in the Square.

I have repeated the procedure also for the Triangle 1 and Triangle 2, defined in Table 4.1. The only difference concerns the definition of region five. In this case, the region is constructed in the same way as before, but taking into account the presence of the oblique cut on the DP. An illustrative example is provided in Figure 4.13, which shows the case of D^0 decays only. It is important to note that for the Triangle 1 $c_i = 0$ for $i = 6 - 10$, and for the Triangle 2 $c_i = 0$ for $i = 1 - 4$.

I reported in Table 4.5 the number of candidates.

Region	Triangle 1	Triangle 2
$n_i + \bar{n}_i$ $[\times 10^3]$	10.3 ± 0.1	44.1 ± 0.2

Table 4.5: Number of reconstructed candidates inside region c_5 in the Triangle 1 and Triangle 2.

In Table 4.6, I reported the expected average asymmetry in the three regions.

Region	Square	Triangle 1	Triangle 2
$\mathcal{A}_{\text{avg}} \times 10^{-4}$	9.4	5.3	12.6

Table 4.6: Expected average asymmetry in different regions of the Dalitz 2.2 ab^{-1}.

The statistical uncertainty sets the limit on the achievable precision. So, before exploring the sources of systematic uncertainties, it is essential to establish whether

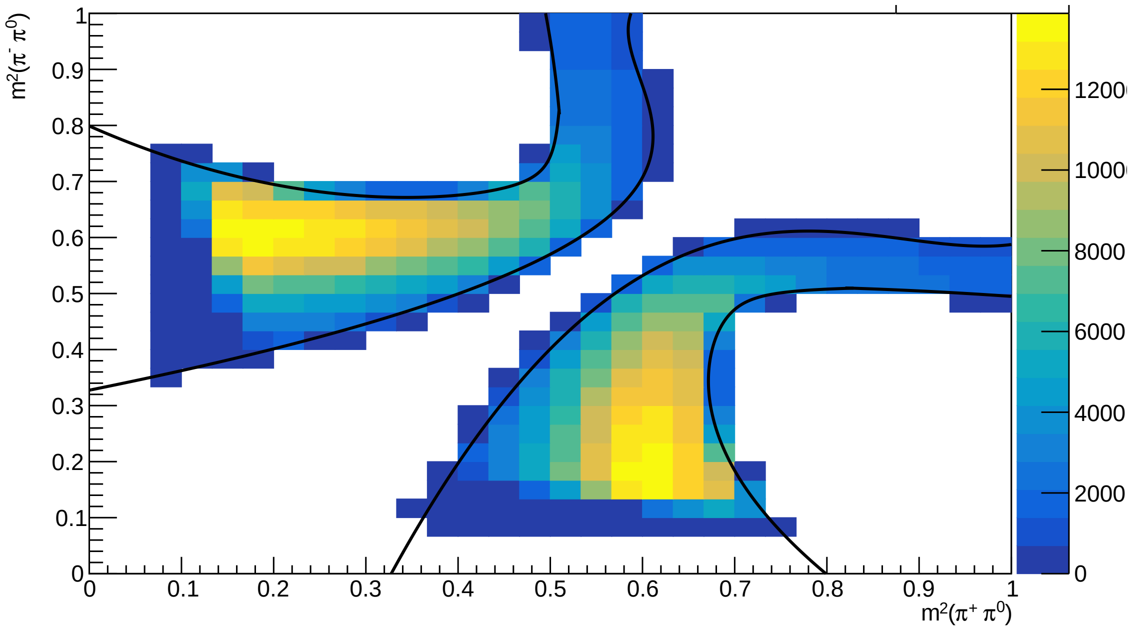

Figure 4.12: Plot of generated events of D^0 and $\bar{D}^0$ decays of the region c_4. 30×30 bins

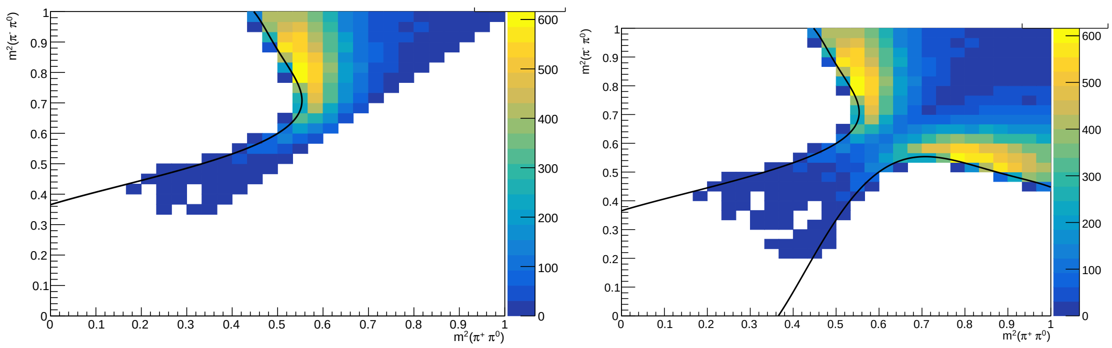

Figure 4.13: Plot of generated events of only D^0 (on the left) and D^0 and $\bar{D}^0$ decays (on the right) inside the region c_5 for the Triangle 2. 30×30 bins.

the available dataset provides sufficient statistical sensitivity to allow for a meaningful measurement of the asymmetry.

4.6 Statistical Uncertainly on A_{CP} and Significance

The statistical uncertainty associated with the raw asymmetry, defined in Equation (3.4), can be expressed as

$$\sigma_{stat} = \frac{2}{n_{tot}^2}\sqrt{n^2\,\sigma_{\bar{n}}^2 + \bar{n}^2\,\sigma_n^2}, \tag{4.4}$$

where n ($\bar{n}$) denotes the number of D^0 ($\bar{D}^0$) events, independent from each other, the $n_{tot} = n + \bar{n}$ is the total event yield, and σ_n ($\sigma_{\bar{n}}$) is the statistical uncertainty associated with $n(\bar{n})$. In the case of purely statistical fluctuations, the uncertainties reduce to the standard Poisson expressions $\sigma_n = \sqrt{n}$ and $\sigma_{\bar{n}} = \sqrt{\bar{n}}$, yielding to

$$\sigma_{\text{stat}} = \frac{2}{n_{\text{tot}}^2}\sqrt{n^2\,\bar{n} + \bar{n}^2\,n}\,. \tag{4.5}$$

When considering prospects, it is natural to evaluate how the sensitivity of the analysis may evolve with increasing the integrated luminosity. Such a projection provides a first indication of the statistical improvements achievable in the future. In particular, a larger integrated luminosity directly translates into a higher precision in the CP asymmetry measurements. Using the fact that σ_{stat} scales as $1/\sqrt{n_{\text{tot}}}$, and n_{tot} scales with the luminosity, I computed the statistical uncertainty for different values of integrated luminosity, and reported these results in Table 4.7.

Region	$\sigma_{\text{stat}} \times 10^{-4}$ [2.2 ab^{-1}]	$\sigma_{\text{stat}} \times 10^{-4}$ [10 ab^{-1}]	$\sigma_{\text{stat}} \times 10^{-4}$ [50 ab^{-1}]
Square	17	8.0	3.5
Triangle 1	23	11	4.8
Triangle 2	24	11	5.0

Table 4.7: Statistical uncertainty at different values of integrated luminosity.

In Table 4.8 I present the values of the *statistical significance*, defined as

$$\mathcal{S}_{\text{stat}} \equiv \frac{\mathcal{A}_{\text{avg}}}{\sigma_{\text{stat}}}, \tag{4.6}$$

and evaluated for integrated luminosities of 50 ab^{-1} and 2.2 ab^{-1}.

Because the $\pi^{\pm}$ of the D^0 and $\bar{D}^0$ have different momentum distributions in a particular region of the Dalitz, the Triangles are highly dependent on charge asymmetries in detection, as mentioned in Section 3.5.2. So, I focused on the Square, because it is the only region that is not affected by ulterior asymmetries due to the detection. Table 4.9 reports the predicted integrated luminosity required to achieve different target values of significance.

Region	$\mathcal{S}_{\text{stat}}$ [2.2 ab^{-1}]	$\mathcal{S}_{\text{stat}}$ [50 ab^{-1}]
Square	0.55	2.7
Triangle 1	0.23	1.1
Triangle 2	0.53	2.5

Table 4.8: Significance of expected average asymmetry in different regions of the Dalitz at different values of integrated luminosity.

The results indicate that at 50 ab^{-1}, the sensitivity is below three standard deviations, considering only the statistical uncertainty. To achieve at least 3 sigma, it is necessary to reduce statistical uncertainty. In practical terms, this corresponds to increasing the number of reconstructed $D^0(\bar{D}^0)$ decays into three pions.

$\mathcal{S}_{\text{stat}}$	0.55	2.7	3	5
L_{int} [ab^{-1}]	2.2	50	62	172

Table 4.9: Significance of expected average asymmetry in the Square of the Dalitz at different values of integrated luminosity.

4.7 Relaxing cuts

I performed a study relaxing some of the selection criteria. In particular, the lower momentum threshold on the π^0 candidate $|\vec{p}| > 500\,\text{MeV/c}$ was removed. This method produced a second dataset, referred to as "relaxed sample". The corresponding statistical differences, both in the full Dalitz plot and in its low-energy region, and the reconstruction efficiency, are summarized in Table 4.10.

Selection Criteria	n_{tot} [$\times 10^6$]	Sample Efficiency ε [%]
Full		
Standard	1.621 ± 0.001	12.66 ± 0.01
Standard [50 ab^{-1}]	36.950 ± 0.006	
Relaxed	1.872 ± 0.001	14.86 ± 0.01
Relaxed [50 ab^{-1}]	43.437 ± 0.007	
Square		
Standard	0.356 ± 0.001	8.28 ± 0.01
Standard [50 ab^{-1}]	8.208 ± 0.003	
Relaxed	0.524 ± 0.001	12.20 ± 0.02
Relaxed [50 ab^{-1}]	12.107 ± 0.003	

Table 4.10: Table of the efficiency of the sample for standard and relaxed selection criteria of the full Dalitz plot and the Square. $n_{\text{tot}} = n_{D^0} + n_{\bar{D}^0}$ is the total number of correctly reconstructed candidates of signal.

The expected number of reconstructed events at higher luminosities can be extrapolated, maintaining the efficiency constant, by scaling the current event yield proportionally to the integrated luminosity. In Table 4.11, I reported how the statistical uncertainty changes for the standard and relaxed samples, for different values of integrated luminosity, and for the Dalitz regions, along with the statistical significance.

For the relaxed sample, the luminosities at which 3 and 5 σ_{stat} would be reached are reported in Table 4.12.

The statistical gain obtained by removing the cut is not so modest; indeed, we could reach 3 σ_{stat} with the goal dataset of Belle II.

This work has shown that reaching a statistical significance of 3 σ_{stat} would require relaxing the selection, and this may affect some other aspects of the analysis,

Selection Criteria	L_{int} [ab^{-1}]	σ_{stat} [$\times 10^{-4}$]	$\mathcal{S}_{\text{stat}}$
Full			
Standard	2.2	8.0	
Relaxed	2.2	5.2	
Standard	50	1.7	
Relaxed	50	1.5	
Square			
Standard	2.2	17	0.55
Relaxed	2.2	14	0.67
Standard	50	3.5	2.7
Relaxed	50	2.9	3.2

Table 4.11: Table of the statistical uncertainty for standard and relaxed selection criteria of the full Dalitz plot and the Square of the reconstructed candidates at different values of integrated luminosity.

$\mathcal{S}_{\text{stat}}$	0.67	3	3.2	5
L_{int} [ab^{-1}]	2.2	44	50	122

Table 4.12: Statistical significance of expected average asymmetry in the Square of the Dalitz for the candidates with relaxing selection, at different values of integrated luminosity.

in particular, the background levels will increase, so the feasibility of the measurement is not guaranteed. We highlight, though, that we have used a single theoretical prediction, while alternative theoretical models may predict larger CP-violating effects. In addition, if there is physics beyond the Standard Model, the value of $\mathcal{A}_{\text{CP}}$ may be further enhanced and the significance increased. Moreover, this work has shown discussed methodology that may be applied to investigate other three-body decays.

Chapter 5

Conclusions

This final chapter summarizes the results and discusses possible analysis strategies to reduce the statistical uncertainty.

5.1 Future Prospects

In this work, the approaches I employed to increase the statistical significance are:

1) **Relax kinematics selection** on the π^0 momentum.

2) **Prediction at higher integrated luminosity** to access the reach at the integrated luminosity goal of Belle II.

Beyond these methods, other strategies can also be investigated. For instance, D^0 mesons reconstructed from D^* decays, where the flavour is determined by the presence of the slow tagging pion, constitute only about 25% of the total number of D^0 mesons produced in an $e^+e^- \to c\bar{c}$ event. Consequently, it is natural to consider additional sources of neutral D mesons, such as:

3) **Charm Flavour Tagging (CFT) method:** this technique employs a binary classifier to assign a probability to the flavour of a neutral D meson by exploiting global information from the entire $e^+e^- \to c\bar{c}$ event. Its main limitation lies in the tagging efficiency, which reaches only about 50% [59].

4) $\boldsymbol{D^0}$ **mesons from** $\boldsymbol{B}$ **decays:** these provide an additional source of signal events, although they introduce different challenges, such as the CP violation of the B mesons, and experimental asymmetries that effect D mesons from B in a different way than D from D^*.

Besides the statistical uncertainty, the systematic error may play an important role, especially at higher luminosities. In particular, the cancellation of the forward-backward asymmetry and the correction of the detection asymmetries are connected with systematic uncertainties. The method usually deployed to remove these nuisance asymmetries from $\mathcal{A}_{\text{raw}}$ is a data-driven method; therefore, we expect that the main part of the systematic uncertainty will scale with statistics. We should note, however, that at higher luminosities we might see additional systematic errors (related or not) to $\mathcal{A}_{\text{det}}$ and $\mathcal{A}_{\text{FB}}$. So one of the next steps on this analysis would be to look at systematic uncertainties and evaluate whether or not these will be the limiting ones of the total uncertainty on $\mathcal{A}_{\text{CP}}$.

5.2 Conclusions

In this thesis, I presented the sensitivity study of the CP asymmetry measurement in the $D^0 \to \pi^+\pi^-\pi^0$ decay channel, using the simulated dataset produced by the Belle II collaboration, corresponding to an integrated luminosity of 2.2 ab^{-1}. I described the formalism behind the CP violation, especially for neutral meson systems, and the importance of this measure inside the SM framework. I exploited the observable $\mathcal{A}_{\text{CP}}$ to study the CPV in the three-body decay $D^0 \to \pi^+\pi^-\pi^0$, and the Dalitz plot as a powerful tool to analyse the distributions of the D^0 and $\bar{D}^0$ decays. Then, after a study of the reconstruction efficiency on different regions of the DP, I focus on the low-energy region of the π^0 to evaluate the CP predicted asymmetry from the theoretical model presented in [37]. I defined three regions: the Square and the Triangles, more sensitive to possible CP violation, due to the interference between $\rho^{\pm}(770)$ resonances. Then, I computed the expected value of the CP asymmetry in the three regions. Finally, I compared the statistical significance of the Belle II simulated dataset to various scenarios of integrated luminosity on the Square, the less sensitive region to experimental asymmetries. The results I found with standard selection criteria are:

$$\mathcal{S}_{\text{stat}} = 0.55 \quad \text{for} \quad L_{\text{int}} = 2.2 \text{ ab}^{-1} \ ; \tag{5.1}$$
$$\mathcal{S}_{\text{stat}} = 3 \quad \text{for} \quad L_{\text{int}} = 62 \text{ ab}^{-1} \ ; \tag{5.2}$$
$$\mathcal{S}_{\text{stat}} = 5 \quad \text{for} \quad L_{\text{int}} = 172 \text{ ab}^{-1} \ . \tag{5.3}$$

For the relaxed sample, without the cut $|\vec{p}(\pi^0)| > 500$ MeV/c, I found:

$$\mathcal{S}_{\text{stat}} = 0.67 \quad \text{for} \quad L_{\text{int}} = 2.2 \text{ ab}^{-1} \ ; \tag{5.4}$$
$$\mathcal{S}_{\text{stat}} = 3 \quad \text{for} \quad L_{\text{int}} = 44 \text{ ab}^{-1} \ ; \tag{5.5}$$
$$\mathcal{S}_{\text{stat}} = 5 \quad \text{for} \quad L_{\text{int}} = 122 \text{ ab}^{-1} \ . \tag{5.6}$$

Considering the specific theoretical model in [37], and with the standard selection criteria, which are reliable against backgrounds and other effects since they have been used in a recent Belle II analysis, the significance at 50 ab^{-1} is below 3 σ_{stat}. Having said that, the method presented in this work is still relevant: in fact, there can be different theoretical models with larger CPV expected, and with a similar method, it is possible to investigate different decay channels.

Appendix A

Selection Criteria

Table A.1, list the skimming criteria, while Table A.2. The main differences are the requirement of a kinematic fit (*KFit*) of the π^0 to identify the $D^0 \to K^+K^-\pi^0$ decay, and the use of a neural network (KIDNN) to evaluate the probability that a reconstructed track corresponds to a kaon.

Particle	Variable	Criteria
Photons		
	clusterNHits	> 1.5
	θ	in range (17°, 150°), within CDC acceptance
	E	> 25 MeV for forward and barrel ECL,
	E	> 40 MeV for backward ECL
Neutral pions		
	M	in range (105, 150) MeV/c^2
	KFit probability	> 0 (fit must converge)
Charged particles		
	d_r	< 1 cm
	$\lvert\mathrm{d}_z\rvert$	< 3 cm
	θ	in range (17°, 150°), within CDC acceptance
	πIDNN	> 0.1
	KIDNN	> 0.1
$\boldsymbol{D^0}$ **mesons**		
	M	in range $(1.7, 2.1)$ GeV/c^2
$\boldsymbol{D^*}$ **mesons**		
	ΔM	< 160 MeV/c^2
	p_{CM}	> 2 GeV/c

Table A.1: Skimming criteria for photons, neutral pions, tracks, and mesons.

Particles	Variable	Criteria
Charged particles	d_r	< 0.5 cm
	$\|d_z\|$	< 1 cm
	θ	in range $(17^{\circ}, 150^{\circ})$
	πIDNN	> 0.2 (D^0 daughters)
	πIDNN	> 0.1 (tag pions)
Photons	θ	in range $(17^{\circ}, 150^{\circ})$
	E	> 100 MeV
	clusterNHits	> 1.5
	|clusterTime|	< 200 ns
	|clusterTimeSignificance|	< 2
	E_1/E_9	> 0.3
	E_9/E_{21}	> 0.8
	clusterZernikeMVA	> 0.1
$\boldsymbol{\pi^0}$ **meson**	M	in range (116, 150) MeV/c^2
	$\| \vec{p} \|$	> 500 MeV/c
$\boldsymbol{D^0}$ **meson**	M	in range (1.785, 1.95) GeV/c^2
$\boldsymbol{D^*}$ **meson**	ΔM	in range $(140, 150)$ MeV/c^2
	X	> 1.06
	TreeFitter	must converge
	Best candidate selection	candidate with highest TreeFit prob

Table A.2: Selection criteria for tracks, mesons, and photons.

Bibliography

[1] G. Steigman. "When clusters collide: constraints on antimatter on the largest scales". In: *Journal of Cosmology and Astroparticle Physics* 2008.10 (Oct. 2008), p. 001. ISSN: 1475-7516. DOI: 10.1088/1475-7516/2008/10/001. URL: http://dx.doi.org/10.1088/1475-7516/2008/10/001.

[2] A. D. Sakharov. "Baryon asymmetry of the universe". In: *Soviet Physics Uspekhi* 34.5 (May 1991), p. 417. DOI: 10.1070/PU1991v034n05ABEH002504. URL: https://dx.doi.org/10.1070/PU1991v034n05ABEH002504.

[3] A. Cohen, A. De Rújula, and S. Glashow. "A Matter-Antimatter Universe?" In: *The Astrophysical Journal* 495.2 (Mar. 1998), pp. 539–549. ISSN: 1538-4357. DOI: 10.1086/305328. URL: http://dx.doi.org/10.1086/305328.

[4] J. Dunkley et al. "FIVE-YEARWILKINSON MICROWAVE ANISOTROPY PROBEOBSERVATIONS: LIKELIHOODS AND PARAMETERS FROM THEWMAP-DATA". In: *The Astrophysical Journal Supplement Series* 180.2 (Feb. 2009), pp. 306–329. ISSN: 1538-4365. DOI: 10.1088/0067-0049/180/2/306. URL: http://dx.doi.org/10.1088/0067-0049/180/2/306.

[5] A. D. Sakharov. "Violation of CP invariance, C asymmetry, and baryon asymmetry of the universe". In: *Soviet Physics Uspekhi* 34.5 (May 1991), p. 392. DOI: 10.1070/PU1991v034n05ABEH002497. URL: https://dx.doi.org/10.1070/PU1991v034n05ABEH002497.

[6] A. Purcell. "Go on a particle quest at the first CERN webfest". In: 35/2012 (2012), p. 10. URL: https://cds.cern.ch/record/1473657.

[7] S. Weinberg. "A Model of Leptons". In: *Phys. Rev. Lett.* 19 (21 Nov. 1967), pp. 1264–1266. DOI: 10.1103/PhysRevLett.19.1264. URL: https://link.aps.org/doi/10.1103/PhysRevLett.19.1264.

[8] S. N. et al. "Review of Particle Physics". In: *Phys. Rev. D* 110 (3 Aug. 2024). https://link.aps.org/doi/10.1103/PhysRevD.110.030001, p. 030001. DOI: 10.1103/PhysRevD.110.030001. URL: https://link.aps.org/doi/10.1103/PhysRevD.110.030001.

[9] C. Grojean, ed. *2012 European School of High-Energy Physics*. 8 lectures, 296 pages [1-29], published as CERN Yellow Report https://cds.cern.ch/record/1406310. CERN. Geneva: CERN, 2014, pp. 1–29. DOI: 10.5170/CERN-2014-008. URL: https://cds.cern.ch/record/1406310.

[10] N. Cabibbo. "Unitary Symmetry and Leptonic Decays". In: *Phys. Rev. Lett.* 10 (12 June 1963), pp. 531–533. DOI: 10.1103/PhysRevLett.10.531. URL: https://link.aps.org/doi/10.1103/PhysRevLett.10.531.

[11] M. Kobayashi and T. Maskawa. “CP-Violation in the Renormalizable Theory of Weak Interaction”. In: *Progress of Theoretical Physics* 49.2 (Feb. 1973), pp. 652–657. ISSN: 0033-068X. DOI: 10.1143/PTP.49.652. eprint: https://academic.oup.com/ptp/article-pdf/49/2/652/5257692/49-2-652.pdf. URL: https://doi.org/10.1143/PTP.49.652.

[12] L. Wolfenstein. “Parametrization of the Kobayashi-Maskawa Matrix”. In: *Phys. Rev. Lett.* 51 (21 Nov. 1983), pp. 1945–1947. DOI: 10.1103/PhysRevLett.51.1945. URL: https://link.aps.org/doi/10.1103/PhysRevLett.51.1945.

[13] C. Jarlskog. “Commutator of the Quark Mass Matrices in the Standard Electroweak Model and a Measure of Maximal CP Nonconservation”. In: *Phys. Rev. Lett.* 55 (10 Sept. 1985). https://link.aps.org/doi/10.1103/PhysRevLett.55.1039, pp. 1039–1042. DOI: 10.1103/PhysRevLett.55.1039. URL: https://link.aps.org/doi/10.1103/PhysRevLett.55.1039.

[14] G. Luders. “On the Equivalence of Invariance under Time Reversal and under Particle-Antiparticle Conjugation for Relativistic Field Theories”. In: *Kong. Dan. Vid. Sel. Mat. Fys. Med.* 28N5.5 (1954), pp. 1–17. URL: https://cds.cern.ch/record/1071765.

[15] G. Lüders. “Proof of the TCP theorem”. In: *Annals of Physics* 2.1 (1957), pp. 1–15. ISSN: 0003-4916. DOI: https://doi.org/10.1016/0003-4916(57)90032-5. URL: https://www.sciencedirect.com/science/article/pii/0003491657900325.

[16] L. Landau. “On the conservation laws for weak interactions”. In: *Nuclear Physics* 3.1 (1957), pp. 127–131. ISSN: 0029-5582. DOI: https://doi.org/10.1016/0029-5582(57)90061-5. URL: https://www.sciencedirect.com/science/article/pii/0029558257900615.

[17] J. H. Christenson et al. “Evidence for the 2π Decay of the K_2^0 Meson”. In: *Phys. Rev. Lett.* 13 (4 July 1964), pp. 138–140. DOI: 10.1103/PhysRevLett.13.138. URL: https://link.aps.org/doi/10.1103/PhysRevLett.13.138.

[18] B. Collaboration. “Direct CP Violating Asymmetry in $B^0 \to K^+\pi^-$ Decays”. In: *Phys. Rev. Lett.* 93 (13 Sept. 2004), p. 131801. DOI: 10.1103/PhysRevLett.93.131801. URL: https://link.aps.org/doi/10.1103/PhysRevLett.93.131801.

[19] B. Collaboration. “Measurement of CP observables in $B^\pm \to D_{CP}K^\pm$ decays and constraints on the CKM angle γ”. In: *Phys. Rev. D* 82 (7 Oct. 2010), p. 072004. DOI: 10.1103/PhysRevD.82.072004. URL: https://link.aps.org/doi/10.1103/PhysRevD.82.072004.

[20] B. Collaboration. “Evidence for Direct CP Violation in $B^0 \to K^+\pi^-$Decays”. In: *Phys. Rev. Lett.* 93 (19 Nov. 2004), p. 191802. DOI: 10.1103/PhysRevLett.93.191802. URL: https://link.aps.org/doi/10.1103/PhysRevLett.93.191802.

[21] B. Collaboration. “Evidence for direct CP violation in the decay $B^{\pm} \to D^{(*)}K^{\pm}$, $D \to K^0_S\pi^+\pi^-$ and measurement of the CKM phase ϕ_3”. In: *Phys. Rev. D* 81 (11 June 2010), p. 112002. DOI: 10.1103/PhysRevD.81.112002. URL: https://link.aps.org/doi/10.1103/PhysRevD.81.112002.

[22] L. Collaboration. “Observation of CP violation in B±→DK± decays”. In: *Physics Letters B* 712.3 (2012), pp. 203–212. ISSN: 0370-2693. DOI: https://doi.org/10.1016/j.physletb.2012.04.060. URL: https://www.sciencedirect.com/science/article/pii/S0370269312004893.

[23] L. Collaboration. “First Observation of CP Violation in the Decays of B^0_s Mesons”. In: *Phys. Rev. Lett.* 110 (22 May 2013), p. 221601. DOI: 10.1103/PhysRevLett.110.221601. URL: https://link.aps.org/doi/10.1103/PhysRevLett.110.221601.

[24] L. Collaboration. “Observation of CP Violation in Charm Decays”. In: *Phys. Rev. Lett.* 122 (21 May 2019), p. 211803. DOI: 10.1103/PhysRevLett.122.211803. URL: https://link.aps.org/doi/10.1103/PhysRevLett.122.211803.

[25] V. Weisskopf and E. Wigner. “Über die natürliche Linienbreite in der Strahlung des harmonischen Oszillators”. In: *Zeitschrift für Physik* 65.1 (Nov. 1930), pp. 18–29. ISSN: 0044-3328. DOI: 10.1007/BF01397406. URL: https://doi.org/10.1007/BF01397406.

[26] A. Karan. “Dealing with T and CPT violations in mixing as well as direct and indirect CP violations for neutral mesons decaying to two vectors”. In: *The European Physical Journal C* 80.8 (2020), p. 782. ISSN: 1434-6052. DOI: 10.1140/epjc/s10052-020-8297-8. URL: https://doi.org/10.1140/epjc/s10052-020-8297-8.

[27] R. H. Dalitz. “CXII. On the analysis of τ-meson data and the nature of the τ-meson”. In: *The London, Edinburgh, and Dublin Philosophical Magazine and Journal of Science* 44.357 (1953), pp. 1068–1080. DOI: 10.1080/14786441008520365. URL: https://doi.org/10.1080/14786441008520365.

[28] R. H. Dalitz. “Decay of τ Mesons of Known Charge”. In: *Physical Review* 94.4 (May 1954), pp. 1046–1051. DOI: 10.1103/PhysRev.94.1046. URL: https://link.aps.org/doi/10.1103/PhysRev.94.1046.

[29] A. J. Bevan and others. “The Physics of the B Factories”. In: *The European Physical Journal C* 74.11 (2014), p. 3026. DOI: 10.1140/epjc/s10052-014-3026-9. URL: https://doi.org/10.1140/epjc/s10052-014-3026-9.

[30] G. N. Fleming. “Recoupling Effects in the Isobar Model. I. General Formalism for Three-Pion Scattering”. In: *Physical Review* 135.2B (July 1964), B551–B560. DOI: 10.1103/PhysRev.135.B551. URL: https://link.aps.org/doi/10.1103/PhysRev.135.B551.

[31] D. J. Herndon, P. Söding, and R. J. Cashmore. “Generalized isobar model formalism”. In: *Physical Review D* 11.11 (June 1975), pp. 3165–3182. DOI: 10.1103/PhysRevD.11.3165. URL: https://link.aps.org/doi/10.1103/PhysRevD.11.3165.

[32] Particle Data Group. *Review of Particle Physics 2024: Resonances*. Revised August 2023 by D. M. Asner, C. Hanhart, and M. Mikhasenko. Aug. 2024. URL: https://pdg.lbl.gov/2024/reviews/rpp2024-rev-resonances.pdf (visited on 09/08/2025).

[33] J. Back et al. "Laura++: A Dalitz plot fitter". In: *Computer Physics Communications* 231 (2018), pp. 198–242. ISSN: 0010-4655. DOI: 10.1016/j.cpc.2018.04.017. URL: https://www.sciencedirect.com/science/article/pii/S0010465518301334.

[34] B. Aubert et al. "Measurement of CP Violation Parameters with a Dalitz Plot Analysis of $B^{\pm} \to D_{\pi^+\pi^-\pi^0} K^{\pm}$". In: *Physical Review Letters* 99.25 (Dec. 2007), p. 251801. DOI: 10.1103/PhysRevLett.99.251801. URL: https://link.aps.org/doi/10.1103/PhysRevLett.99.251801.

[35] Y. Grossman and S. Schacht. "U-spin sum rules for CP asymmetries of three-body charmed baryon decays". In: *Phys. Rev. D* 99 (3 Feb. 2019), p. 033005. DOI: 10.1103/PhysRevD.99.033005. URL: https://link.aps.org/doi/10.1103/PhysRevD.99.033005.

[36] Y. Grossman and S. Schacht. "The emergence of the $\Delta U = 0$ rule in charm physics". In: *Journal of High Energy Physics* 2019.7 (2019), p. 20. ISSN: 1029-8479. DOI: 10.1007/JHEP07(2019)020. URL: https://doi.org/10.1007/JHEP07(2019)020.

[37] A. Dery et al. "Probing the $\Delta U = 0$ rule in three body charm decays". In: *Journal of High Energy Physics* 2021.5 (2021), p. 179. ISSN: 1029-8479. DOI: 10.1007/JHEP05(2021)179. URL: https://doi.org/10.1007/JHEP05(2021)179.

[38] J.-E. Augustin et al. "Discovery of a Narrow Resonance in e^+e^- Annihilation". In: *Physical Review Letters* 33.23 (Dec. 1974), pp. 1406–1408. DOI: 10.1103/PhysRevLett.33.1406. URL: https://link.aps.org/doi/10.1103/PhysRevLett.33.1406.

[39] J. J. Aubert et al. "Experimental Observation of a Heavy Particle J". In: *Physical Review Letters* 33.23 (Dec. 1974), pp. 1404–1406. DOI: 10.1103/PhysRevLett.33.1404. URL: https://link.aps.org/doi/10.1103/PhysRevLett.33.1404.

[40] S. W. Herb et al. "Observation of a Dimuon Resonance at 9.5 GeV in 400-GeV Proton-Nucleus Collisions". In: *Physical Review Letters* 39.5 (Aug. 1977), pp. 252–255. DOI: 10.1103/PhysRevLett.39.252. URL: https://link.aps.org/doi/10.1103/PhysRevLett.39.252.

[41] N. S. Lockyer et al. "Measurement of the Lifetime of Bottom Hadrons". In: *Physical Review Letters* 51.15 (Oct. 1983), pp. 1316–1319. DOI: 10.1103/PhysRevLett.51.1316. URL: https://link.aps.org/doi/10.1103/PhysRevLett.51.1316.

[42] H. Albrecht et al. "Observation of B0-B0 mixing". In: *Physics Letters B* 192.1 (1987), pp. 245–252. ISSN: 0370-2693. DOI: https://doi.org/10.1016/0370-2693(87)91177-4. URL: https://www.sciencedirect.com/science/article/pii/0370269387911774.

[43] K. Kinoshita. “Reflections on beauty1Talk presented at A Symposium in Honor of the 65th Birthday of Professor P. Buford Price.1”. In: *New Astronomy Reviews* 42.3 (1998), pp. 263–270. ISSN: 1387-6473. DOI: https://doi.org/10.1016/S1387-6473(98)00011-6. URL: https://www.sciencedirect.com/science/article/pii/S1387647398000116.

[44] P. F. Harrison and H. R. Quinn. “The BABAR Physics Book: Physics at an Asymmetric B Factory, Chap. 3, Table 3-1, p. 75”. In: *Papers from Workshop on Physics at an Asymmetric B Factory*. Ed. by P. F. Harrison and H. R. Quinn. BaBar Collaboration Meeting, Rome, Italy, 11–14 Nov 1996; Princeton, NJ, 17–20 Mar 1997; Orsay, France, 16–19 Jun 1997; Pasadena, CA, 22–24 Sep 1997. SLAC, 1998. URL: https://www.slac.stanford.edu/pubs/slacreports/slac-r-504.html.

[45] T. Abe et al. *Belle II Technical Design Report*. Technical Design Report. KEK, Nov. 2010. arXiv: 1011.0352 [physics.ins-det]. URL: https://arxiv.org/abs/1011.0352.

[46] Belle II Collaboration. *Belle II Official Website*. 2025. URL: https://www.belle2.org/ (visited on 09/01/2025).

[47] D. Matvienko. “The Belle II experiment: status and physics program”. In: *EPJ Web of Conferences* 191 (Jan. 2018), p. 02010. DOI: 10.1051/epjconf/201819102010.

[48] T. Kuhr et al. “The Belle II Core Software”. In: *Computing and Software for Big Science* 3.1 (2018), p. 1. ISSN: 2510-2044. DOI: 10.1007/s41781-018-0017-9. URL: https://doi.org/10.1007/s41781-018-0017-9.

[49] V. Bertacchi et al. “Track finding at BelleII”. In: *Computer Physics Communications* 259 (2021), p. 107610. ISSN: 0010-4655. DOI: https://doi.org/10.1016/j.cpc.2020.107610. URL: https://www.sciencedirect.com/science/article/pii/S0010465520302861.

[50] W. Altmannshofer et al. “The Belle II Physics Book”. In: *PTEP* 2019.12 (2019). Ed. by E. Kou and P. Urquijo. [Erratum: PTEP 2020, 029201 (2020)], p. 123C01. DOI: 10.1093/ptep/ptz106. arXiv: 1808.10567 [hep-ex].

[51] D. J. Lange. “The EvtGen particle decay simulation package”. In: *Nuclear Instruments and Methods in Physics Research Section A: Accelerators, Spectrometers, Detectors and Associated Equipment* 462.1 (2001). BEAUTY2000, Proceedings of the 7th Int. Conf. on B-Physics at Hadron Machines, pp. 152–155. ISSN: 0168-9002. DOI: 10.1016/S0168-9002(01)00089-4. URL: https://www.sciencedirect.com/science/article/pii/S0168900201000894.

[52] E. Barberio, B. van Eijk, and Z. Wąs. “Photos — a universal Monte Carlo for QED radiative corrections in decays”. In: *Computer Physics Communications* 66.1 (1991), pp. 115–128. ISSN: 0010-4655. DOI: 10.1016/0010-4655(91)90012-A. URL: https://www.sciencedirect.com/science/article/pii/001046559190012A.

[53] S. Jadach, B. Ward, and Z. Wąs. "The precision Monte Carlo event generator KK for two-fermion final states in e^+e^- collisions". In: *Computer Physics Communications* 130.3 (2000), pp. 260–325. ISSN: 0010-4655. DOI: 10.1016/S0010-4655(00)00048-5. URL: https://www.sciencedirect.com/science/article/pii/S0010465500000485.

[54] T. Sjöstrand et al. "An introduction to PYTHIA 8.2". In: *Computer Physics Communications* 191 (2015), pp. 159–177. ISSN: 0010-4655. DOI: 10.1016/j.cpc.2015.01.024. URL: https://www.sciencedirect.com/science/article/pii/S0010465515000442.

[55] S. Agostinelli et al. "Geant4—a simulation toolkit". In: *Nuclear Instruments and Methods in Physics Research Section A: Accelerators, Spectrometers, Detectors and Associated Equipment* 506.3 (2003), pp. 250–303. ISSN: 0168-9002. DOI: 10.1016/S0168-9002(03)01368-8. URL: https://www.sciencedirect.com/science/article/pii/S0168900203013688.

[56] R. Brun and F. Rademakers. "ROOT — An object oriented data analysis framework". In: *Nuclear Instruments and Methods in Physics Research Section A: Accelerators, Spectrometers, Detectors and Associated Equipment* 389.1 (1997). New Computing Techniques in Physics Research V, pp. 81–86. ISSN: 0168-9002. DOI: 10.1016/S0168-9002(97)00048-X. URL: https://www.sciencedirect.com/science/article/pii/S016890029700048X.

[57] M. Artuso et al. "Charm meson spectra in e^+e^- annihilation at 10.5-GeV c.m.e." In: *Phys. Rev. D* 70 (2004), p. 112001. DOI: 10.1103/PhysRevD.70.112001. arXiv: hep-ex/0402040.

[58] L. Massaccesi and S. Robertson. "Mixing and CP-violation measurements with D mesons at Belle and BelleII". In: *Proceedings of EPS-HEP 2025*. Contribution 154543, Indico, IN2P3. URL: https://indico.in2p3.fr/event/33627/contributions/154543/.

[59] Adachi et al. "Novel method for the identification of the production flavor of neutral charmed mesons". In: *Phys. Rev. D* 107 (11 June 2023), p. 112010. DOI: 10.1103/PhysRevD.107.112010. URL: https://link.aps.org/doi/10.1103/PhysRevD.107.112010.